

Nested spheroidal figures of equilibrium

II. Generalization to \mathcal{L} layers

J.-M. Huré^{1,2*}

¹Univ. Bordeaux, LAB, UMR 5804, F-33615, Pessac, France

²CNRS, LAB, UMR 5804, F-33615, Pessac, France

Received ??? / Accepted ???

ABSTRACT

We present a vectorial formalism to determine the approximate solutions to the problem of a composite body made of \mathcal{L} homogeneous, rigidly rotating layers bounded by spheroidal surfaces. The method is based on the 1st-order expansion of the gravitational potential over confocal parameters, thereby generalizing the method described in Paper I for $\mathcal{L} = 2$. For a given relative geometry of the ellipses and a given set of mass-density jumps at the interfaces, the sequence of rotation rates and interface pressures is obtained analytically by recursion. A wide range of equilibria result when layers rotate in an asynchronous manner, although configurations with a negative oblateness gradient are more favorable. In contrast, states of global rotation (all layers move at the same rate), found by solving a linear system of $\mathcal{L} - 1$ equations, are much more constrained. In this case, we mathematically demonstrate that confocal and coelliptical configurations are not permitted. Approximate formula for small ellipticities are derived. These results reinforce and prolongate known results and classical theorems restricted to small ellipticities. Comparisons with the numerical solutions computed from the Self-Consistent-Field method are successful.

Key words: Gravitation — stars: interiors — stars: rotation — Methods: analytical

1 INTRODUCTION

The theory of figures, indisputably, is among the most important production in theoretical astrophysics that has occupied mathematicians and physicists for more than two centuries (Chandrasekhar 1969; Hachisu 1986; Horedt 2004; Tohline 2021). Since the pionnering contributions by Newton, Maclaurin, Jacobi and others, it has undergone various extensions and remains a reference to understand the structure of stars, planets, asteroids and even galaxies. In these contexts, the question of stratification in mass and in rotation is fundamental (e.g. Schönberg & Chandrasekhar 1942; Maeder 1971; Rambaux et al. 2015; Cisneros-Parra et al. 2019). The equilibrium of a heterogeneous body made of homogeneous layers bounded by pure spheroidal surfaces has been soon investigated, with a special interest for the Earth and planets (Poincaré 1888; Love et al. 1914). According to Poincaré’s theorem, only confocal configurations are compatible with solid rotation and lead to exact solutions. These states, however, require a mass-density inversion and seem therefore of minor interest (Hamy 1890; Montalvo et al. 1983). As quoted by Hamy (1889), approximate solutions are compatible with rigid rotation for small ellipticities,

which situation is traditionnally reached in the slow-rotation limit. Véronet (1912) has discussed the possibility of asynchronously rotating layers; see also Montalvo et al. (1983). In the present article, we reconsider Hamy’s idea by expanding the gravitational potential over *confocal parameters* (instead of ellipticities), and include the hypothesis that layers are eventually in relative motion. As the degrees of freedom are increased, a larger diversity of equilibria follows. The approach is purely analytical. Numerical solutions remains technically tricky to obtain when mass-density jumps and rotational discontinuities are both present (Kiuchi et al. 2010; Kadam et al. 2016; Basillais & Huré 2021). Actually, the surfaces bounding layers more or less deviate from pure spheroids and do not match with the standard coordinate systems. In addition, for classic computational grids, Poisson-solvers have generally poor efficiency in the presence of sharp density profiles.

We generalize the approach presented in Huré (2021) (hereafter, Paper I) devoted to the 2-layer problem, by considering \mathcal{L} homogeneous layers in relative orbital motion. We mainly determine the rotation rates of each layer, the interface pressures and the central pressure as a function of the mass densities in the layers and the geometry of the spheroids (ellipticities and fractional radii). As for the two-layer case, the formalism resides on the expansion of

* E-mail:jean-marc.hure@u-bordeaux.fr

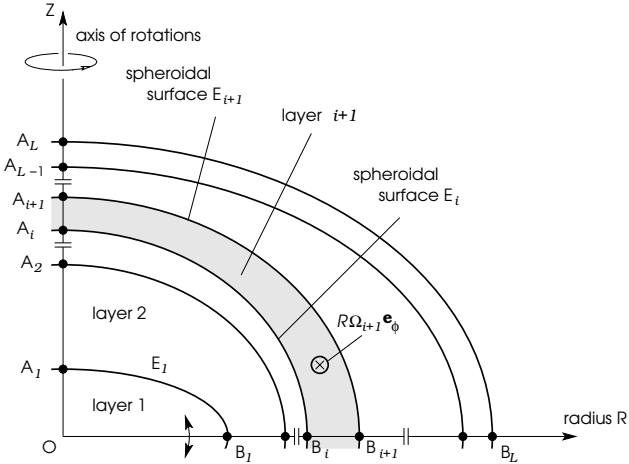


Figure 1. Typical configuration for a nested structure made of \mathcal{L} homogeneous layers (the deepest one is layer number 1) bounded by oblate spheroidal surfaces. At each interface E_i , a mass-density jump and a rotational discontinuity are present; see (24a) and Sect. 2.4.

the gravitational potential in the confocal parameters. Two classes of solutions can be distinguished, depending on the run of the gas pressure (constant or variable) along the interfaces: the ones associated with global rotation and the others corresponding to asynchronously rotating layers, respectively. The pertinent equations of problem, and in particular the conditions required for approximate rigid rotations, are presented in Sect. 2. The sequence of rotation rates $\{\Omega_1, \dots, \Omega_{\mathcal{L}}\}$, which is obtained by recursivity, is established in Sect. 3. The problem is then recast in a compact, vectorial form. We briefly discuss the conditions for obtaining real rotation rates. Section 4.3 is devoted to examples. Two configurations of special interest, namely the confocal and coelliptical states, are analyzed. The solutions obtained numerically from the Self-Consistent-Field (SCF) method with the multi-layer DROP-code (Basillais & Huré 2021) are used in comparison. We show in Sect. 5 how to treat the special case of global rotation (all layers share the same rotation rate). In Sect. 6, we derive the zero-order approximations for the Ω_i 's valid for small ellipticities. The interface pressures along the rotation axis are given in the Appendix A. The two-layer case is reproduced in the Appendix B. A basic Fortran 90 program that computes the sequence of rotation rates and the polar pressure at the interfaces is available in the Appendix C. A summary and a few perspectives are found in the last section.

2 THE EQUATIONS OF EQUILIBRIUM

2.1 Theoretical background. Notations

We adopt the same theoretical background and the same notations as in Paper I. We consider \mathcal{L} oblate spheroidal surfaces $E_i(a_i, b_i)$ with semi-minor axis b_i and semi-major axis $a_i > b_i$, with $i \in [1, \mathcal{L}]$, sharing the same axis of revolution and same plane of symmetry (and subsequently the same centre). Each surface E_i (except the outermost one $E_{\mathcal{L}}$) is fully contained into a larger one E_{i+1} , i.e. $b_i < b_{i+1}$ and $a_i < a_{i+1}$, producing a nested structure as depicted

in Fig. 1. The deepest one, bounded by E_1 , has index 1, while the outermost layer, bounded by $E_{\mathcal{L}-1}$ and $E_{\mathcal{L}}$, has index \mathcal{L} . Intersecting surfaces are excluded (see e.g. Caimmi 2016). If we introduce the fractional radius $q_{i,j} = a_i/a_j$, the immersion conditions write

$$\begin{cases} \bar{\epsilon}_{i+1} - q_{i,i+1}\bar{\epsilon}_i \geq 0, \\ q_{i,i+1} \leq 1, \end{cases} \quad i = 1, \dots, \mathcal{L} - 1 \quad (1a)$$

where $b_i/a_i = \bar{\epsilon}_i$ is the dimensionless polar radius (or axis ratio) of E_i . While some constraints will be set in the sequel, there is no hypothesis yet on the ellipticities

$$\epsilon_i = \sqrt{1 - \bar{\epsilon}_i^2}, \quad (2)$$

which are allowed to differ from one surface to the other. These \mathcal{L} surfaces define \mathcal{L} domains (or layers), which are all homogeneous. If ρ_i denotes the mass density of layer number i , the mass fractions ν_i are given by¹

$$M\nu_i = \frac{4}{3}\pi a_{\mathcal{L}}^3 \begin{cases} \rho_1 \bar{\epsilon}_1 q_{1,\mathcal{L}}^3, & i = 1, \\ \rho_i (q_{i,\mathcal{L}}^3 \bar{\epsilon}_i - q_{i-1,\mathcal{L}}^3 \bar{\epsilon}_{i-1}), & i \in [2, \mathcal{L}], \end{cases} \quad (3)$$

where M is the total mass. In these conditions, the equilibrium of layer $i \in [1, \mathcal{L}]$ is governed by the Bernoulli equation (Lyttleton 1953)

$$\frac{p_i}{\rho_i} + \Phi_i + \Psi = \text{const.}_i, \quad (4)$$

where p_i is the pressure of matter, $\Phi_i = -\int \Omega_i^2(R)RdR$ is the centrifugal potential, R is the cylindrical radius, $\Omega_i(R)$ is the rotation rate, and Ψ is the total gravitational potential. For practical reasons (the centrifugal force vanishes on the rotation axis), the constant in the right-hand-side is preferentially determined at $R = 0$. The other decisive equations come from the requirement of pressure balance at the connection between any pair of adjacent layers, namely

$$p_{i+1}|_{E_i} = p_i|_{E_i}, \quad i \in [1, \mathcal{L} - 1]. \quad (5)$$

For the outermost surface, we have $p_{\mathcal{L}}|_{E_{\mathcal{L}}} = 0$ in the absence of any ambient pressure p_a (we take $p_a = 0$ in the paper throughout). In fact, this latter surface condition can be incorporated into (5) if the ambient medium is regarded as a supplementary layer, with number $\mathcal{L} + 1$ and null pressure $p_a = p_{\mathcal{L}+1} = 0$. Finally, the Poisson equation, which yields Ψ from the mass-density field, is the last equation (see below). There are $2\mathcal{L} + 1$ equations in total.

2.2 The total gravitational potential

The potential in (4) is the major source of complexity as it requires, in general, to solve the Poisson equation (Clement 1974; Hachisu 1986). However, the fact that all bounding surfaces are, in any meridional plane, perfect ellipses brings a significant simplification since a closed form exceptionally exists in such a case. Actually, let us remind that the potential in space due to a homogeneous body (with mass density ρ) bounded by a spheroidal surface $E(a, b)$ can be

¹ As suggested by the referee, an extra layer (with index 0) null size and null mass can be placed at the center of the coordinates. This would enable to merge the two formula in (3) into a single expression provided $q_{0,\mathcal{L}} = 0$. Then, we would have $\lambda \equiv R^2 + Z^2$ and $f = 0$ in (6), and the sum in (9) could start at $i = 1$.

written in the following compact form (Chandrasekhar 1969; Binney & Tremaine 1987)

$$\frac{\Psi(R, Z)}{-\pi G \rho} = f [A_0(\epsilon')(a^2 + \lambda) - A_1(\epsilon')R^2 - A_3(\epsilon')Z^2], \quad (6)$$

where

$$\left\{ \begin{array}{l} A_0(\epsilon) = 2 \frac{\bar{\epsilon}}{\epsilon} \arcsin \epsilon, \\ A_1(\epsilon) = \frac{\bar{\epsilon}}{\epsilon^3} [\arcsin \epsilon - \epsilon \bar{\epsilon}], \\ A_3(\epsilon) = -2 \frac{\bar{\epsilon}}{\epsilon^3} \left[\arcsin \epsilon - \frac{\epsilon}{\bar{\epsilon}} \right], \\ f = \frac{a^2 b}{(a^2 + \lambda) \sqrt{b^2 + \lambda}}, \\ \epsilon'^2 = 1 - \frac{b^2 + \lambda}{a^2 + \lambda}, \end{array} \right. \quad (7a)$$

$$\quad (7b)$$

$$\quad (7c)$$

$$\quad (7d)$$

$$\quad (7e)$$

and λ is defined by

$$\left\{ \begin{array}{l} \lambda = 0, \quad \text{inside the body and onto } E, \\ \frac{R^2}{a^2 + \lambda} + \frac{Z^2}{b^2 + \lambda} - 1 = 0, \\ \text{outside the body.} \end{array} \right. \quad (8a)$$

$$\quad (8b)$$

This formula therefore works indifferently inside and outside the body. In (8b), λ is the largest root of the second degree polynomial. Although not explicitly quoted, this quantity (and subsequently f and ϵ') depend on R and Z outside E , with a and b as parameters. On this basis, the total potential of the nested structure is easily derived from the superposition principle by using (6) $2\mathcal{L} - 1$ times with appropriate settings for the parameters a and b of the ellipses in the sample, as each layer (except the deepest one) is bounded by two surfaces. We therefore have (see note 1)

$$\begin{aligned} \frac{\Psi(R, Z)}{-\pi G} = \sum_{i=2}^{\mathcal{L}} \rho_i \{ & f_i [A_0(\epsilon'_i)(a_i^2 + \lambda_i) - A_1(\epsilon'_i)R^2 \\ & - A_3(\epsilon'_i)Z^2] - f_{i-1} [A_0(\epsilon'_{i-1})(a_{i-1}^2 + \lambda_{i-1}) - A_1(\epsilon'_{i-1})R^2 \\ & - A_3(\epsilon'_{i-1})Z^2] \} + \rho_1 f_1 [A_0(\epsilon'_1)(a_1^2 + \lambda_1) - A_1(\epsilon'_1)R^2 \\ & - A_3(\epsilon'_1)Z^2], \end{aligned} \quad (9)$$

where λ_i , f_i and ϵ'_i are still defined according to (8a)-(8b), (7d) and (7e) respectively, but (a, b) must be replaced by (a_i, b_i) .

Given the objectives of the article, the potential is not needed everywhere in space, but only along each spheroid E_i in the sample. More precisely, we have to consider pairs (E_i, E_j) of surfaces. Let $\lambda_{i,j}$ designate the values of λ_i associated with the spheroid i bounded by $E_i(a_i, b_i)$ taken along $E_j(a_j, b_j)$, i.e. $\lambda_{i,j} = \lambda_i(E_j)$. In a similar way, $f_{i,j}$ and $\epsilon'_{i,j}$ stand respectively for f_i , ϵ_i evaluated onto $E_j(a_j, b_j)$. As R and Z along E_j are linked by

$$Z^2 = b_j^2(1 - \varpi_j^2), \quad (10)$$

where $\varpi_j = R/a_j$, we see that $\lambda_{i,j}$ depends on a single space variable, for instance the radius, i.e. $\lambda_{i,j} \equiv \lambda_{i,j}(\varpi_j)$ which, in turn, depends on 3 parameters b_j , a_i and b_i .

2.3 The confocal parameters

Although we will leave (9) in its actual form, the summation can be split into two terms: one term corresponding to the

potential of all layers located above a given layer j in the sample (including the layer itself), and one term for the total potential of all layers located below it. This separation is explicit in the dissertation by Hamy (1889). Actually, we see from (7d) and (7e) that, if $E_j \subset E_i$, which occurs for $j \leq i$, then $f_{i,j} = 1$ and $\epsilon'_{i,j} = \epsilon_i$ since $\lambda_{i,j} = 0$. On the contrary, if E_j is exterior to E_i , which occurs for $j > i$, then $\lambda_{i,j}$ must be calculated from (8b) for any term of the summation. This second situation is the main source of difficulty.

For convenience, the quadratic equation in $\lambda_{i,j}$ is rewritten in terms of the new variable $x_{i,j}$ defined by

$$x_{i,j} a_j^2 = a_i^2 + \lambda_{i,j}, \quad (11)$$

and so, according to (8b), the relevant root is given by

$$x_{i,j} = \frac{1}{2} (1 + c_{i,j} + \epsilon_j^2 \varpi_j^2) + \frac{1}{2} \sqrt{(1 + c_{i,j} + \epsilon_j^2 \varpi_j^2)^2 - 4q_{i,j}^2 \epsilon_i^2 \varpi_j^2}, \quad (12)$$

where

$$c_{i,j} = q_{i,j}^2 \epsilon_i^2 - \epsilon_j^2 \quad (13)$$

is the *confocal parameter* associated with the pair (E_i, E_j) . There are \mathcal{L}^2 parameters of this kind in total. Note that any surface is confocal with itself, i.e. $c_{i,i} = 0$. We see that, if E_i is confocal with E_j , then $x_{i,j} = 1$ since $c_{i,j} = 0$, which just means that $\lambda_{i,j}$ is a constant. Otherwise, $x_{i,j}$ varies along E_j . We have $x_{i,j} = 1 + c_{i,j}$ at point A_j of the polar axis and $x_{i,j} = 1$ at point B_j of the equatorial plane (see Fig. 1). By rearranging the summation in (9), the total potential at a radius $R = \varpi_j a_j$ onto E_j , denoted $\Psi(E_j, \varpi_j)$ from now on, can be rewritten as

$$\begin{aligned} \frac{\Psi(E_j, \varpi_j)}{-\pi G a_{\mathcal{L}}^2 q_{\mathcal{L}, \mathcal{L}}^2} = \sum_{i=1}^{\mathcal{L}-1} (\rho_i - \rho_{i+1}) f_{i,j} [& A_0(\epsilon'_{i,j}) x_{i,j} \\ & - A_1(\epsilon'_{i,j}) \varpi_j^2 - A_3(\epsilon'_{i,j}) \epsilon_j^2 (1 - \varpi_j^2)] \\ + \rho_{\mathcal{L}} [& A_0(\epsilon'_{\mathcal{L}, j}) x_{\mathcal{L}, j} - A_1(\epsilon'_{\mathcal{L}, j}) \varpi_j^2 - A_3(\epsilon'_{\mathcal{L}, j}) \epsilon_j^2 (1 - \varpi_j^2)], \end{aligned} \quad (14)$$

where we have used (10), and

$$\left\{ \begin{array}{l} x_{i,j} = q_{i,j}^2 \\ f_{i,j} = 1, \end{array} \right. \quad (15a)$$

$$\quad (15b)$$

$$\left\{ \begin{array}{l} \epsilon'_{i,j} = \epsilon_i \quad \text{if } E_j \subseteq E_i \text{ (or } j \leq i), \\ \text{or} \end{array} \right. \quad (15c)$$

$$\left\{ \begin{array}{l} x_{i,j} \text{ from (12) — see below,} \end{array} \right. \quad (15d)$$

$$\left\{ \begin{array}{l} f_{i,j} = \frac{q_{i,j}^3 \bar{\epsilon}_i}{x_{i,j} \sqrt{x_{i,j} - q_{i,j}^2 \epsilon_i^2}}, \end{array} \right. \quad (15e)$$

$$\left\{ \begin{array}{l} \epsilon'_{i,j} = \frac{q_{i,j} \epsilon_i}{\sqrt{x_{i,j}}} \quad \text{if } E_i \subset E_j \text{ (or } j > i). \end{array} \right. \quad (15f)$$

Note that the last term in the right-hand-side of (14) can be simplified since $E_{\mathcal{L}}$ is always external to all other surfaces, meaning $\epsilon'_{\mathcal{L}, j} = \epsilon_{\mathcal{L}}$ for any $j \in [1, \mathcal{L}]$.

2.4 The conditions for approximate rigid rotations

Since (12) is not quadratic in R and $\epsilon'_{i,j}$ are not constants, the centrifugal potentials Φ_i in (4) cannot, in general, be pure functions of R^2 , which would correspond to strict, rigid rotations. Thus, we see that there is no exact solution to the problem of nested figures of equilibrium for rigid rotations

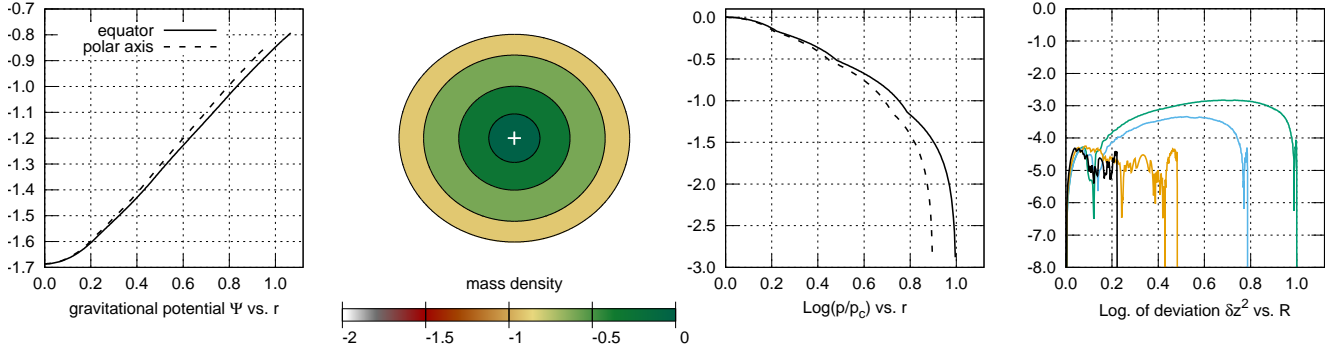


Figure 2. Equilibrium solution computed for $\mathcal{L} = 4$ with the DROP-code for configuration A (see Tab. 1 for the input parameter set and results). All layers rotate at the same rate (global rotation). *From left to right* (in log. scale): the gravitational potential at the pole (*dashed line*) and at the equator (*plain line*), the normalized mass-density ρ/ρ_c in color code, the normalized pressure p/p_c and absolute deviations between the “true” surfaces and the ellipses E_i .

configuration A (input)				
layer	$i = 1$	2	3	4
$\leftarrow q_{i,4}\bar{\epsilon}_i$	0.21	0.45	0.72	0.9
$\leftarrow \rho_i/\rho_{i+1}$	2	2	2	

	DROP-code	this work	
$q_{1,4}$	0.22176		
$q_{2,4}$	0.48230		
$q_{3,4}$	0.78690		
ϵ_1	0.32141		
ϵ_2	0.35984		
ϵ_3	0.40349		
$c_{1,4}$	-0.18491		
$c_{2,4}$	-0.15987		
$c_{3,4}$	-0.08918		
$V/a_{\mathcal{L}}^3$	3.76482	3.76991	
$p_c/\pi G\rho_4 a_4^2$	6.22120	6.22023	
$p_1^*/\pi G\rho_4 a_4^2$	4.23407	4.23393	
$p_2^*/\pi G\rho_4 a_4^2$	1.89163	1.89159	
$p_3^*/\pi G\rho_4 a_4^2$	0.45253	0.45271	
$\bar{\Omega}_1^2$	0.13002	0.13347	0.13446 ^a
$\bar{\Omega}_2^2$	0.13002	0.13046	0.12795 ^a
$\bar{\Omega}_3^2$	0.13002	0.13020	0.12514 ^a
$\bar{\Omega}_4^2$	0.13002	0.13016	0.12389 ^a
$M/\rho_4 a_4^3$	6.68126	6.68742	
ν_1	0.05178	0.05175	
ν_2	0.23664	0.23639	
ν_3	0.42743	0.42737	

*value on the polar axis

^afrom (53) and (54)

Table 1. Input and output data for configuration A ($\mathcal{L} = 4$) associated with Fig. 2 obtained with the DROP-code (column 2; see text) and from the actual formalism (columns 3 and 4); see notes 2 and 3; see also Sect. 4.3. Numbers are truncated.

if the bounding surfaces are perfect ellipsoids of revolution. This is not a new result. The exception is for configurations where $c_{i,j} = 0$ for all pairs of surfaces, the so-called confocal configurations (Poincaré 1888). In such a case, because the $\lambda_{i,j}$'s, and subsequently the f_i 's and the ϵ_i 's are all constants, the “coefficients” A_0 , A_1 and A_3 in (7a)-(7c) do not depend on R and Z , and are “true” constants. As pointed

out in Paper I, there is another possibility: the presence of an ambient pressure acting at $E_{\mathcal{L}}$ can help to produce a series of rigid rotations in the system. This pressure has to absorb or compensate all terms in the potential at $E_{\mathcal{L}}$ of degree equal (optional) or higher than R^2 . If some residuals remain, the compensation must continue down to the innermost surface E_1 . As quoted above, we work with $p_a = 0$.

As considered soon by Hamy (1889), approximate solutions compatible with rigid rotation can be derived in the case of small ellipticities, which corresponds to slow rotations. By rigid rotation, we mean that each layer has its own solid body motion (implying a rotational discontinuity Ω_i/Ω_{i+1} at each surface E_i). As in Paper I, we go beyond this hypothesis by assuming

$$|c_{i,j}| \ll 1 \quad (i,j) \in [1, \mathcal{L}]^2, \quad (16)$$

which is more general than the combined conditions $\epsilon_j^2 \ll 1$ and $\epsilon_j^2 \ll 1$. Under these circumstances, we have from (12)

$$x_{i,j} \approx 1 + c_{i,j}(1 - \varpi_j^2), \quad (17)$$

in the first-order (see Paper I). At order zero in $c_{i,j}$, we have $x_{i,j} = 1$, and the $\lambda_{i,j}$'s are all constants, as well as all quantities in (7a)-(7e). At order 1, $x_{i,j}$ is quadratic with the radius and we have in particular

$$\begin{cases} x_{i,j}|_{A_j} = 1 + c_{i,j}, \\ x_{i,j}|_{B_j} = 1. \end{cases} \quad (18)$$

at the two end-points A_j and B_j of E_j (see Fig. 1; see again Paper I for more details).

We show in Fig. 2 an example² of a nested figure of equilibrium obtained with 4 layers (i.e. $\mathcal{L} = 4$) with the DROP-code that solves the full problem³ by numerical means from

² In the graphs and tables, the pressure is given in units of $\pi G\rho_{\mathcal{L}}^2 a_{\mathcal{L}}^2$, the rotation rates are given in units of $\sqrt{2\pi G\rho_{\mathcal{L}}}$ and the potential is in units of $\pi G\rho_{\mathcal{L}} a_{\mathcal{L}}^2$.

³ In the DROP-code, the interfaces at equilibrium are automatically detected all along the convergence cycle, which guarantees a good accuracy of various integrals involved (i.e., boundary conditions and global, output quantities). In its current version, the location of points B_i in the equatorial plane is not known in advance. Like the ellipticities and fractional radii, these are outputs. In practice, we have adopted resolution of $1/256^2$, which

the Self-Consistent-Field (SCF) method (Basillais & Huré 2021). The rigid rotation law is used, and all layers rotate at the same rate here (rotation is global). Table 1 contains all input parameters (ellipticities, mass-density jumps and fractional sizes) and the main output quantities (interface pressure, rotation rate, fractional masses, etc.; see note 2). Unsurprisingly, the interfaces are not perfect ellipses, mainly because the true gravitational potential is not strictly given by (9). The deviations shown in Fig. 2, in Z^2 , are, however, less than 10^{-3} in absolute for all the surfaces involved. The confocal parameters are negative, less than 0.19 in absolute. These results indicate that the hypothesis of nested figures of equilibrium based on spheroidal surfaces and approximate rigid rotations is fully justified (more examples below).

3 SOLUTIONS

As long as the approximation of rigid rotation holds, the solution to the problem is obtained from (4), (5) and (9). It is fully analytical. As in Paper I, we can determine the interface pressures at $R = 0$ where the centrifugal force vanishes. This is summarized in the Appendix A.

3.1 The sequence of rotation rates

The rotation rate of the top layer is obtained first, because $E_{\mathcal{L}}$ is a surface of null pressure. From (4) evaluated at the two end-points $A_{\mathcal{L}}$ and $B_{\mathcal{L}}$, where $\varpi_{ij} = 0$ and 1 respectively, and by using (14) for $j = \mathcal{L}$, we find after subtraction

$$-\frac{1}{2}\Omega_{\mathcal{L}}^2 a_{\mathcal{L}}^2 + \Psi(E_{\mathcal{L}}, 1) - \Psi(E_{\mathcal{L}}, 0) = 0, \quad (19)$$

which leads to

$$\begin{aligned} \frac{\Omega_{\mathcal{L}}^2}{2\pi G} &= \rho_{\mathcal{L}} [A_1(\epsilon_{\mathcal{L}}) - A_3(\epsilon_{\mathcal{L}})\epsilon_{\mathcal{L}}^2] \\ &- \sum_{i=1}^{\mathcal{L}-1} (\rho_i - \rho_{i+1}) \left\{ f_{i\mathcal{L}} [A_0(\epsilon'_{i,j})x_{i\mathcal{L}} - A_3(\epsilon'_{i,j})\epsilon_{\mathcal{L}}^2] \right\} \Big|_{A_{\mathcal{L}}}^{B_{\mathcal{L}}} \\ &+ \sum_{i=1}^{\mathcal{L}-1} (\rho_i - \rho_{i+1}) \left\{ f_{i\mathcal{L}} [A_1(\epsilon'_{i\mathcal{L}}) - A_3(\epsilon'_{i\mathcal{L}})\epsilon_{\mathcal{L}}^2] \right\} \Big|_{B_{\mathcal{L}}}. \end{aligned} \quad (20)$$

The first term inside the brackets in the right-hand-side is nothing but the Maclaurin function

$$\mathcal{M}(\epsilon) = A_1(\epsilon) - (1 - \epsilon^2)A_3(\epsilon), \quad (21)$$

corresponding to a single Maclaurin spheroid bounded by $E_{\mathcal{L}}$ (see Paper I). The other terms come from the embedded layers (with mass density in excess of $\rho_{\mathcal{L}}$). These can be expressed by using the intermediate functions \mathcal{P} and \mathcal{C} already defined in Paper I, namely

$$\mathcal{M}(\epsilon)\mathcal{P}(\epsilon, \epsilon') = A_3(\epsilon')(1 - \epsilon^2) - A_1(\epsilon'), \quad (22)$$

and

$$\mathcal{M}(\epsilon)\mathcal{C}(\epsilon, \epsilon') = A_0(\epsilon')x - (1 - \epsilon^2)A_3(\epsilon'), \quad (23)$$

is reached for 8 levels of multigrid. Numbers in the tables are therefore limited to 5 digits, and truncated.

where x is linked to λ according to (11). On this basis, and with the supplementary definitions

$$\alpha_i = \frac{\rho_i}{\rho_{i+1}}, \quad (24a)$$

$$\tilde{\rho}_i = \frac{\rho_i}{\rho_{\mathcal{L}}}, \quad (24b)$$

$$\tilde{\Omega}_i^2 = \frac{\Omega_i^2}{2\pi G \rho_{\mathcal{L}}}, \quad (24c)$$

we see that (20) becomes

$$\begin{aligned} \tilde{\Omega}_{\mathcal{L}}^2 &= \mathcal{M}(\epsilon_{\mathcal{L}}) \left\{ 1 - \sum_{i=1}^{\mathcal{L}-1} \tilde{\rho}_{i+1}(\alpha_i - 1) f_{i\mathcal{L}} \mathcal{P}(\epsilon_{\mathcal{L}}, \epsilon'_{i,\mathcal{L}}) \Big|_{B_{\mathcal{L}}} \right. \\ &\left. - \sum_{i=1}^{\mathcal{L}-1} \tilde{\rho}_{i+1}(\alpha_i - 1) \underbrace{f_{i\mathcal{L}} \mathcal{C}(\epsilon_{\mathcal{L}}, \epsilon'_{i,\mathcal{L}}) \Big|_{A_{\mathcal{L}}}^{B_{\mathcal{L}}}}_{\text{corrections}} \right\}, \quad (25) \end{aligned}$$

where $\mathcal{P}(\epsilon_{\mathcal{L}}, \epsilon'_{i,\mathcal{L}}) \Big|_{B_{\mathcal{L}}} = \mathcal{P}(\epsilon_{\mathcal{L}}, q_{i,\mathcal{L}}\epsilon_{i,\mathcal{L}})$. As evoked already, if E_i and $E_{\mathcal{L}}$ are confocal, then $x_{i,\mathcal{L}} = 1$ both at $A_{\mathcal{L}}$ and $B_{\mathcal{L}}$ for a given i , with the consequence that $f_{i\mathcal{L}} \mathcal{C}(\epsilon_{\mathcal{L}}, \epsilon'_{i,\mathcal{L}}) \Big|_{A_{\mathcal{L}}}^{B_{\mathcal{L}}} = 0$. The last summation therefore represents the series of 1st-order corrections with respect to confocal configurations. It is expected to be small if all the $c_{i,j}$'s are close to zero. Note that the amplitude of each corrective term with respect to the corresponding leading one does not depend on α_i but just on the geometry of the pair of ellipses involved.

Once $\tilde{\Omega}_{\mathcal{L}}^2$ is known, we can deduce the rotation rate of all layers down to the centre by recursion, as follows. If we multiply the Bernoulli equation for layer $j < \mathcal{L}$ by the mass-density jump α_j at the interface with layer $j+1$ where $p_j = p_{j+1}$ along E_j by virtue of (5), we get from (4)

$$\begin{aligned} \frac{1}{2} (\Omega_{j+1}^2 - \alpha_j \Omega_j^2) R^2 + (\alpha_j - 1) \Psi(E_j, \varpi_j) \\ + \text{const.}_{j+1} - \alpha_j \text{const.}_j = 0, \end{aligned} \quad (26)$$

where $\Psi(E_j, \varpi_j)$ is given by (14). The two constants are easily eliminated by evaluating this expression at the two end-points of the surface E_j , namely at point A_j where $\varpi_j = 0$ and at point B_j where $\varpi_j = 1$ (see Fig. 1). After some algebra and simplification by $q_{j,\mathcal{L}}^2 \neq 0$, we get

$$\begin{aligned} \frac{\tilde{\Omega}_{j+1}^2 - \alpha_j \tilde{\Omega}_j^2}{\alpha_j - 1} \\ - \sum_{i=1}^{\mathcal{L}-1} \tilde{\rho}_{i+1}(\alpha_i - 1) \left\{ f_{i,j} [A_0(\epsilon'_{i,j})x_{i,j} - A_1(\epsilon'_{i,j})] \right\} \Big|_{B_j} \\ + \sum_{i=1}^{\mathcal{L}-1} \tilde{\rho}_{i+1}(\alpha_i - 1) \left\{ f_{i,j} [A_0(\epsilon'_{i,j})x_{i,j} - A_3(\epsilon'_{i,j})\epsilon_j^2] \right\} \Big|_{A_j} \\ + f_{\mathcal{L},j} [A_0(\epsilon'_{\mathcal{L},j})x_{\mathcal{L},j} - A_1(\epsilon'_{\mathcal{L},j})] \Big|_{B_j} \\ - f_{\mathcal{L},j} [A_0(\epsilon'_{\mathcal{L},j})x_{\mathcal{L},j} - A_3(\epsilon'_{\mathcal{L},j})\epsilon_j^2] \Big|_{A_j} = 0 \end{aligned} \quad (27)$$

where $\alpha_j - 1 \neq 0$ (otherwise E_j is not an interface and layers j and $j+1$ merge into a unique domain). The last two terms can be simplified because $j < \mathcal{L}$. Again, after substantial

rearrangements and by using the functions \mathcal{P} and \mathcal{C} , we find

$$\begin{aligned} \alpha_j \tilde{\Omega}_j^2 &= \tilde{\Omega}_{j+1}^2 - (\alpha_j - 1) \mathcal{M}(\epsilon_j) \\ &\times \left\{ \mathcal{P}(\epsilon_j, \epsilon_{\mathcal{L}}) + \sum_{i=1}^{\mathcal{L}-1} \tilde{\rho}_{i+1} (\alpha_i - 1) f_{i,j} \mathcal{P}(\epsilon_j, \epsilon'_{i,j}) \Big|_{B_j} \right. \\ &\quad \left. + \sum_{i=1}^{\mathcal{L}-1} \tilde{\rho}_{i+1} (\alpha_i - 1) f_{i,j} \mathcal{C}(\epsilon_j, \epsilon'_{i,j}) \Big|_{A_{\mathcal{L}}}^{B_{\mathcal{L}}} \right\}, \end{aligned} \quad (28)$$

which form clearly shows the leading term and the first-order correction. As $\mathcal{P}(\epsilon_j, \epsilon_j) = -1$, we see that this expression (28) even works for $j = \mathcal{L}$ if we imagine that the whole nested structure is immersed into an hypothetical medium with extremely low density $\rho_{\mathcal{L}+1} \ll \rho_{\mathcal{L}}$ and rotating at the same rate as the outermost layer \mathcal{L} , i.e. $\tilde{\Omega}_{\mathcal{L}} = \tilde{\Omega}_{\mathcal{L}+1}$ (both sides of the equation then simplify by $\alpha_i - 1 \neq 1$). This medium must not bring any contribution to the total gravity field. This is typically the situation of generalized Roche systems, where a massive body carries away a rarefied gas (e.g. [Jeans 1928](#); [Maeder 2009](#)). In the present case, the rotation rate of this extra, massless component is the rotation rate of the outermost layer \mathcal{L} .

3.2 Vectorial notation

It is clear that (25) and (28) can be regarded as scalar products in a \mathcal{L} -dimension Euclidean space (with, for instance, $\{\mathbf{u}_1, \dots, \mathbf{u}_{\mathcal{L}}\}$ as the natural basis of unit vectors). Actually, if we define the three vectors

$$\mathbf{X} = \frac{1}{\rho_{\mathcal{L}}} \begin{pmatrix} \rho_1 - \rho_2 \\ \rho_2 - \rho_3 \\ \dots \\ \rho_i - \rho_{i+1} \\ \dots \\ \rho_{\mathcal{L}-1} - \rho_{\mathcal{L}} \\ \rho_{\mathcal{L}} \end{pmatrix}, \quad (29)$$

$$\mathbf{P}(B_j) = \begin{pmatrix} f_{1,j} \mathcal{P}(\epsilon_j, \epsilon'_{1,j}) \Big|_{B_j} \\ f_{2,j} \mathcal{P}(\epsilon_j, \epsilon'_{2,j}) \Big|_{B_j} \\ \dots \\ f_{i,j} \mathcal{P}(\epsilon_j, \epsilon'_{i,j}) \Big|_{B_j} \\ \dots \\ f_{\mathcal{L}-1,j} \mathcal{P}(\epsilon_j, \epsilon'_{\mathcal{L}-1,j}) \Big|_{B_j} \\ \mathcal{P}(\epsilon_j, \epsilon'_{\mathcal{L},j}) \Big|_{B_j} \end{pmatrix}, \quad (30)$$

and

$$\mathbf{C}(A_j, B_j) = \begin{pmatrix} f_{1,j} \mathcal{C}(\epsilon_j, \epsilon'_{1,j}) \Big|_{A_j}^{B_j} \\ f_{2,j} \mathcal{C}(\epsilon_j, \epsilon'_{2,j}) \Big|_{A_j}^{B_j} \\ \dots \\ f_{i,j} \mathcal{C}(\epsilon_j, \epsilon'_{i,j}) \Big|_{A_j}^{B_j} \\ \dots \\ f_{\mathcal{L}-1,j} \mathcal{C}(\epsilon_j, \epsilon'_{\mathcal{L}-1,j}) \Big|_{A_j}^{B_j} \\ 0 \end{pmatrix}, \quad (31)$$

then (25) becomes

$$\tilde{\Omega}_{\mathcal{L}}^2 = -\mathcal{M}(\epsilon_{\mathcal{L}}) \mathbf{X} \cdot [\mathbf{P}(B_{\mathcal{L}}) + \mathbf{C}(A_{\mathcal{L}}, B_{\mathcal{L}})]. \quad (32)$$

layer	$i = 1$	2	3	comment
$q_{i,\mathcal{L}}$	0.6	0.7	1	
α_i	1.5	2		
$\rightarrow X_i$	1	1	1	
$\bar{\epsilon}_i$	0.9	0.8	0.7	$\nabla \epsilon > 0$

	$j = 1$	2	3
$\mathcal{M}(\epsilon_j)$	0.05202	0.10067	0.14451
$\mathbf{P}(B_j)$	$\begin{pmatrix} -1 \\ +0.64262 \\ +2.53737 \end{pmatrix}$	$\begin{pmatrix} -1.17636 \\ -1 \\ -0.14791 \end{pmatrix}$	$\begin{pmatrix} -0.90406 \\ -1.15023 \\ -1 \end{pmatrix}$
$\tilde{\Omega}_j^2$	0.22481	0.39393	0.53219

Table 2. Values for $\mathcal{M}(\epsilon_j)$, $\mathbf{P}(B_j)$ and $\tilde{\Omega}_j^2$ obtained from (29), (30), (32) and (33) for a configuration with $\mathcal{L} = 3$. This case corresponds to a positive gradient of ellipticity from the center to the surface of the body.

where we have used $\mathbf{P}(B_{\mathcal{L}}) \cdot \mathbf{u}_{\mathcal{L}} = P_{\mathcal{L}}(B_{\mathcal{L}}) = 1$. From (28), the recurrence relation, for $j \in [1, \mathcal{L} - 1]$, is

$$\begin{aligned} \alpha_j \tilde{\Omega}_j^2 &= \tilde{\Omega}_{j+1}^2 \\ &- (\alpha_j - 1) \mathcal{M}(\epsilon_j) \mathbf{X} \cdot [\mathbf{P}(B_j) + \mathbf{C}(A_j, B_j)]. \end{aligned} \quad (33)$$

For $\mathcal{L} = 2$, we recover the expressions reported in Paper I; see the Appendix B.

3.3 Conditions of positivity

As for $\mathcal{L} = 2$ (see Paper I, and references therein), the positivity of all $\tilde{\Omega}_j^2$'s is not guaranteed at this level. Even if we assume that there is no density inversion from the centre to the surface, the components of vector \mathbf{P} can be positive or negative depending on the relative geometry of the spheroids (see Fig. 4 in Paper I). This point is critical regarding the existence of an equilibrium structure and it must be examined in details for a given set of input parameters (ellipticities ϵ_i , fractional sizes $q_{i,j}$, and mass-density jumps α_i). In the case $\mathcal{L} > 2$, it does not seem easy to make a precise inventory of allowed and forbidden equilibria, because of the high number of parameters involved, $3\mathcal{L} - 2$ in total. First, we expect $\|\mathbf{C}\| \ll \|\mathbf{P}\|$ provided confocal parameters are all small in absolute; see (16). Second, we see from (32) that $\tilde{\Omega}_{\mathcal{L}}^2 > 0$ if the scalar product $\mathbf{X} \cdot \mathbf{P}(B_{\mathcal{L}})$ is negative. For stability reasons, states involving density inversions (i.e. $\alpha_i < 1$) are not desirable. The preference is therefore given to configurations with essentially negative components of $\mathbf{P}(B_{\mathcal{L}})$. By looking at the $\mathcal{P}(\epsilon, \epsilon')$ -graph (again, see Fig. 4 in Paper I), we see that, at order 0, negative values of $\mathcal{P}(\epsilon_{\mathcal{L}}, \epsilon'_{i,\mathcal{L}})$ occur typically when $\epsilon_{\mathcal{L}} \gtrsim \epsilon'_{i,\mathcal{L}}$, i.e. for $c_{i,\mathcal{L}} \lesssim 0$. This condition is automatically fulfilled when $\epsilon_{\mathcal{L}} \gtrsim \epsilon_i \geq q_{i,\mathcal{L}} \epsilon_i$, which corresponds to an outermost spheroid more oblate than all other spheroids. We can use a similar qualitative argument to see what happens below layer \mathcal{L} . Actually, from the recursion formula (33), we see that $\tilde{\Omega}_j^2$ is *unconditionnally positive* if the \mathcal{L} components $P_i(B_j)$ all take negative values. This occurs when $\epsilon_j \gtrsim \epsilon'_{i,j} \geq q_{i,j} \epsilon_i$, i.e. for $c_{i,j} \lesssim 0$ (again, see Fig. 4 in Paper I), namely when the spheroid E_j is more oblate than those located below. The reasoning holds down to the core. Note that this does not depend on the mass-density jumps, provided $\alpha_i > 1$. The most favorable and natural

layer	$i = 1$	2	3	comment
$q_{i,\mathcal{L}}$	0.6	0.7	1	
α_i	1.5	2		
X_i	1	1	1	
$\bar{\epsilon}_i$	0.7	0.8	0.9	$\nabla\epsilon < 0$

	$j = 1$	2	3
$\mathcal{M}(\epsilon_j)$	0.14451	0.10067	0.05202
$\mathbf{P}(\mathbf{B}_j)$	$\begin{pmatrix} -1 \\ -1.515512 \\ -1.96242 \end{pmatrix}$	$\begin{pmatrix} -0.51642 \\ -1 \\ -1.7387 \end{pmatrix}$	$\begin{pmatrix} -0.00780 \\ -0.09029 \\ -1 \end{pmatrix}$
$\tilde{\Omega}_j^2$	0.34618	0.19572	0.06363

Table 3. Same caption as for Tab. 2 but for a negative gradient of ellipticity.

situations for the existence of nested figures are therefore expected for *increasing ellipticities from the center to the surface*, as in the two-layer case. This prolongates the result by Hamy (1889), which is limited to small ellipticities. If we omit the correction, (33) can be put in the form

$$\tilde{\Omega}_{j+1}^2 - \tilde{\Omega}_j^2 \approx (\alpha_j - 1) \left[\tilde{\Omega}_j^2 + \mathcal{M}(\epsilon_j) \mathbf{X} \cdot \mathbf{P}(\mathbf{B}_j) \right]. \quad (34)$$

As a consequence, when $\nabla\epsilon > 0$, $\Omega_{\mathcal{L}}^2$ can be significantly large, while Ω_1^2 is, in contrast, rather small because $P_1(\mathbf{B}_j) \gtrsim 0$ for $j > 1$. It follows that $\tilde{\Omega}_{j+1}^2 - \tilde{\Omega}_j^2$ is expected to be positive, i.e. $\nabla\Omega > 0$. This is illustrated with the data of Tab. 2. Quite logically, the more oblate a layer the faster its rotation rate. This is however not a general rule. Configurations with negative gradients of ellipticity are also permitted. In such a case, $P_1(\mathbf{B}_j) < 0$ typically. The second term in the right-hand side of (34) can be large in absolute (but negative), leading to $\tilde{\Omega}_{j+1}^2 - \tilde{\Omega}_j^2 < 0$. We give in Tab. 3 an example of such a configuration where a negative gradient of ellipticity is associated with a negative gradient of rotation rate. Again, this is not a general rule, just a trend. It immediately follows from this discussion that if the configurations where the rotation rates of all layers are close to each other, i.e. $\nabla\Omega \approx 0$, then the ϵ_j 's can increase or decrease from the center to the surface. As (34) indicates, this is especially true when the α_i 's are all close to unity. However, we do not have $\nabla\epsilon \rightarrow 0$ in the limit $\nabla\Omega \rightarrow 0$, i.e. at global rotation (see below).

4 SPECIAL CASES AND EXAMPLES

4.1 Confocal configurations

For confocal states, $c_{i,j} = 0$ for all pairs (E_i, E_j) of spheroidal surfaces, which means that $\lambda_{i,j} = \text{const.}$ along E_i . In these conditions, we have $\mathbf{C}(A_j, B_j) = \mathbf{0}$, $\mathcal{P}(\epsilon_j, \epsilon'_{i,j}) = -1$ and $f_{i,j} = q_{i,j}^3 \bar{\epsilon}_i / \bar{\epsilon}_j$ at point B_j . We easily show that, for $j = \mathcal{L}$, (32) becomes

$$-\mathbf{X} \cdot \mathbf{P}(\mathbf{B}_{\mathcal{L}}) = \frac{M}{\frac{4}{3}\pi\rho_{\mathcal{L}}a_{\mathcal{L}}^3\bar{\epsilon}_{\mathcal{L}}} \equiv \mu. \quad (35)$$

We see that the denominator in the right-hand-side is just the mass of a (single-component) Maclaurin spheroid having

the same mass-density and same external bounding surface as the outer layer \mathcal{L} of the nested structure. As a consequence, we have $\mu > 1$ provided $\rho_{\mathcal{L}} < \rho_i$ for $i \in [1, \mathcal{L} - 1]$, i.e. the outer layer is less dense than all the interior ones (no density inversion). Let us now determine the rotation rate of the layer located just below, by setting $j = \mathcal{L} - 1$ in the formula. We still have $\mathcal{P}(\epsilon_i, \epsilon'_{i,j}) = -1$ for all components except for the last one, which is $\mathcal{P}(\epsilon_{\mathcal{L}}, \epsilon'_{\mathcal{L}-1,\mathcal{L}}) = \mathcal{P}(\epsilon_{\mathcal{L}}, \epsilon_{\mathcal{L}-1})$. The scalar product in (33) therefore writes

$$-\mathbf{X} \cdot \mathbf{P}(\mathbf{B}_{\mathcal{L}-1}) = \frac{1}{\rho_{\mathcal{L}}} [(\rho_1 - \rho_2)f_{1,\mathcal{L}-1} + (\rho_2 - \rho_3)f_{2,\mathcal{L}-1} + \dots + (\rho_{\mathcal{L}-1} - \rho_{\mathcal{L}}) - \rho_{\mathcal{L}}\mathcal{P}(\epsilon_{\mathcal{L}}, \epsilon_{\mathcal{L}-1})], \quad (36)$$

which can advantageously be rewritten as a function of the total mass, namely

$$-\mathbf{X} \cdot \mathbf{P}(\mathbf{B}_{\mathcal{L}-1}) = \frac{1}{\rho_{\mathcal{L}}a_{\mathcal{L}-1}^3\bar{\epsilon}_{\mathcal{L}-1}} \left\{ \frac{M}{\frac{4}{3}\pi} - \rho_{\mathcal{L}} [a_{\mathcal{L}-1}^3\bar{\epsilon}_{\mathcal{L}-1}\mathcal{P}(\epsilon_{\mathcal{L}}, \epsilon_{\mathcal{L}-1}) + a_{\mathcal{L}}^3\bar{\epsilon}_{\mathcal{L}}] \right\}. \quad (37)$$

Let us now assume that layers $\mathcal{L} - 1$ and \mathcal{L} rotate at the same rate, i.e. $\Omega_{\mathcal{L}} = \Omega_{\mathcal{L}-1}$. From (32) and (33), and given the two scalar products (36) and (37), the condition of synchronous rotation implies

$$f_{\mathcal{L}-1,\mathcal{L}}\mathcal{M}(\epsilon_{\mathcal{L}})\mu - \mathcal{M}(\epsilon_{\mathcal{L}-1}) [\mu - f_{\mathcal{L}-1,\mathcal{L}}\mathcal{P}(\epsilon_{\mathcal{L}}, \epsilon_{\mathcal{L}-1}) - 1] = 0, \quad (38)$$

where

$$f_{\mathcal{L}-1,\mathcal{L}} = \frac{\epsilon_{\mathcal{L}}^3\bar{\epsilon}_{\mathcal{L}-1}}{\epsilon_{\mathcal{L}-1}^3\bar{\epsilon}_{\mathcal{L}}}, \quad (39)$$

by virtue of confocality. If we solve this equation for μ , we get

$$\mu = \frac{\mathcal{M}(\epsilon_{\mathcal{L}-1}) [1 + f_{\mathcal{L}-1,\mathcal{L}}\mathcal{P}(\epsilon_{\mathcal{L}}, \epsilon_{\mathcal{L}-1})]}{\mathcal{M}(\epsilon_{\mathcal{L}-1}) - f_{\mathcal{L}-1,\mathcal{L}}\mathcal{M}(\epsilon_{\mathcal{L}})}, \quad (40)$$

and the question is: do we still have $\mu > 1$? Clearly, this new expression for μ depends on two parameters $\epsilon_{\mathcal{L}-1}$ and $\epsilon_{\mathcal{L}} < \epsilon_{\mathcal{L}-1}$. It is plotted in the form of contour levels in Fig. 3, and we find that μ is always less than unity. This is therefore in contradiction with the above conclusion; see (35). It means that layers $\mathcal{L} - 1$ and \mathcal{L} cannot rotate at the same rate. Note that no value has been assigned to \mathcal{L} here. We therefore confirm that *a heterogeneous body made of homogeneous components separated by confocal spheroids cannot be in global rotation if the mass-density decreases from the center to the surface*, in the conditions of the actual approximation. This generalizes the result obtained by Montalvo et al. (1983) for $\mathcal{L} = 2$; see also Paper I; see Sect. 4.3 for an illustration. Again, this agrees with Hamy (1889).

4.2 Coelliptical configurations

Configurations where all ellipsoidal surfaces have the same ellipticity is of special interest. It is for instance the main assumption made in the model of concentric Maclaurin spheroids (CMS) for planetary interiors (Hubbard 2013). These states are obtained by setting $\epsilon_i = \epsilon$ for $i = [1, \mathcal{L}]$ in the equations. Let us consider the deepest layer, first. From (33) with $j = 1$, we have

$$\alpha_1\tilde{\Omega}_1^2 = \tilde{\Omega}_2^2 - (\alpha_1 - 1)\mathcal{M}(\epsilon) \mathbf{X} \cdot [\mathbf{P}(\mathbf{B}_1) + \mathbf{C}(A_1, B_1)]. \quad (41)$$

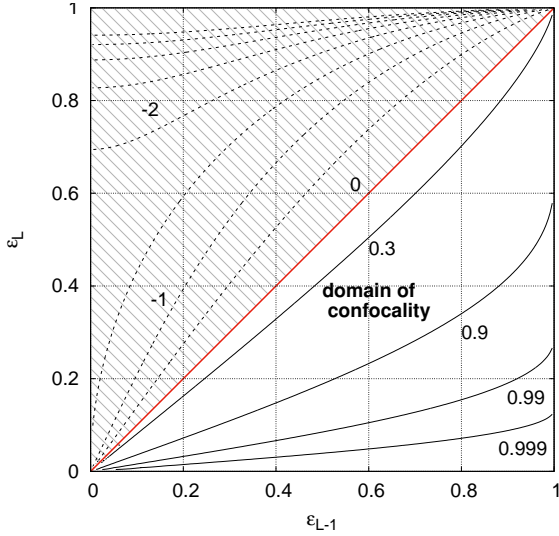


Figure 3. The function $\mu(\epsilon_{\mathcal{L}-1}, \epsilon_{\mathcal{L}})$ defined by (40) in the form of levels of contours (values are labelled on the curves). In the domain relevant for confocality (bottom right-part of the graph), $\mu < 1$, which implies that confocal configurations are not compatible with layers $\mathcal{L}-1$ and \mathcal{L} in synchronous rotation, for a normal/stable stratification of the mass density in the whole structure.

There is no confocal correction for $j = 1$ (whatever the set of ellipticities) since $E_1 \subset E_i$ for all surfaces in the sample. As $\epsilon'_{i,1} = \epsilon_i$ and $f_{i,1} = 1$, we have $\mathcal{P}(\epsilon_1, \epsilon'_{i,1}) = -1$, and it follows that $\mathbf{X} \cdot \mathbf{P}(B_1) = \rho_1/\rho_{\mathcal{L}}$. The rotations rates of the deepest layers are therefore linked by the simple relationship

$$\alpha_1 \tilde{\Omega}_1^2 = \tilde{\Omega}_2^2 + (\alpha_1 - 1) \mathcal{M}(\epsilon) \frac{\rho_1}{\rho_{\mathcal{L}}}. \quad (42)$$

If we consider the surface E_2 which separates the layers 2 and 3 and set $j = 2$ in (33), we get

$$\alpha_2 \tilde{\Omega}_2^2 = \tilde{\Omega}_3^2 - (\alpha_2 - 1) \mathcal{M}(\epsilon) \mathbf{X} \cdot [\mathbf{P}(B_2) + \mathbf{C}(A_2, B_2)]. \quad (43)$$

As above, $f_{i,2} = 1$, $P_i(\epsilon_1, \epsilon'_{i,1}) = -1$ and $C_i(A_2, B_2) = 0$ for any $i > 1$ (because layer 2 is exterior to layer 1). We then have

$$\begin{aligned} -\rho_{\mathcal{L}} \mathbf{X} \cdot [\mathbf{P}(B_2) + \mathbf{C}(A_2, B_2)] = \\ -(\rho_1 - \rho_2) \left[f_{1,2} \mathcal{P}(\epsilon_2, \epsilon'_{1,2}) \Big|_{B_2} + f_{1,2} \mathcal{C}(\epsilon_2, \epsilon'_{1,2}) \Big|_{A_2}^{B_2} \right] \\ + (\rho_2 - \rho_3) + (\rho_3 - \rho_4) + \dots + (\rho_{\mathcal{L}-1} - \rho_{\mathcal{L}}) + \rho_{\mathcal{L}}, \\ = \rho_1 - (\rho_1 - \rho_2) h, \end{aligned} \quad (44)$$

where the function

$$h = 1 + f_{1,2} \mathcal{P}(\epsilon_2, \epsilon'_{1,2}) \Big|_{B_2} + f_{1,2} \mathcal{C}(\epsilon_2, \epsilon'_{1,2}) \Big|_{A_2}^{B_2}, \quad (45)$$

has already been introduced in Paper I. Obviously, $\epsilon_2 = \epsilon$ and $\epsilon'_{1,2}$ depends on q and ϵ , which makes h a function of these two quantities. We see that (43) then takes the form

$$\alpha_2 \tilde{\Omega}_2^2 = \tilde{\Omega}_3^2 + (\alpha_2 - 1) \mathcal{M}(\epsilon) \frac{\rho_1}{\rho_{\mathcal{L}}} \left[1 - \frac{\rho_1 - \rho_2}{\rho_1} h(\epsilon, q) \right]. \quad (46)$$

Let us assume that layers 1 to 3 are in synchronous rotation. We see from (42) with (46) that this is possible only if $h(\epsilon, q) = 0$ somewhere in the range $(\epsilon, q) \in [0, 1]^2$. As shown in Paper I (see Fig. 6), h remains positive in the whole plane, and it vanishes only for $\epsilon = q\epsilon$ (namely $q = 1$,

configuration B (input)			
layer	$i = 1$	2	3
$q_{i,3} \bar{\epsilon}_i$	0.25166	0.42725	0.9
α_i	2	2	

	DR0P-code	this work	
$q_{1,3}$	0.50156	0.50332	
$q_{2,3}$	0.60936	0.61036	
ϵ_1	0.86567	0.86602	
ϵ_2	0.71400	0.71414	
$c_{1,3}$	-0.00061	0	
$c_{2,3}$	-0.00015	0	
V/a_3^3	3.77057	3.76991	
$p_c/\pi G \rho_3 a_3^2$	2.40553	2.40491	
$p_1^*/\pi G \rho_3 a_3^2$	1.48071	1.46845	
$p_2^*/\pi G \rho_3 a_3^2$	0.81826	0.80963	
$\tilde{\Omega}_1^2$	0.76767	0.76690	0.71690 ^a
$\tilde{\Omega}_2^2$	0.30654	0.30623	0.31381 ^a
$\tilde{\Omega}_3^2$	0.06867	0.06859	0.07510 ^a
$M/\rho_3 a_3^3$	4.97044	4.97076	
ν_1	0.21445	0.21489	
ν_2	0.16102	0.16081	

*value on the polar axis

^afrom (53) and (54)

Table 4. Same legend as for Tab. 1 but for configuration B (confocal case, $\mathcal{L} = 3$) shown in Fig. 4.

i.e. layer 2 has null size), which can easily be established from (45). We conclude that layers 1 to 3 cannot rotate at the same rate (as shown in Paper I, synchronous rotation is not possible for $\mathcal{L} = 2$). Note, again, that no value of \mathcal{L} has been specified in the demonstration. We conclude that a *heterogeneous body made of homogeneous components separated by coelliptical/similar spheroids cannot be in global rotation*, in the conditions of the actual approximation. An example is given below. This agrees with Hamy's theorem.

4.3 A few tests. Efficiency and limit of the method

As the first test, we consider the parameter set of Tab. 1 (configuration A). The sequence of rotation rates is computed from (32) and (33) for $j = \{1, 2, 3\}$, and the pressure at the interfaces and at the centre is estimated by recursion from formula given in the Appendix A. As we make systematic comparisons with the numerical solutions obtained from the SCF-method (Basillais & Huré 2021) which is used as “the reference”, it is important that all the formulas are fed with the same parameters (see note 3). For this configuration, the location of points A_i on the polar axis, the mass-density jumps and the fractional radii q_i are the values delivered by the DR0P-code on output. The results are reported in the same table columns 2 and 3). We notice the remarkable agreement between the analytical approach and the numerical reference. The deviations observed for the pressures, rotation rates and fractional masses are of the order of a few 10^{-3} in relative.

The second and third tests illustrate the two cases considered in Sects. 4.1 and 4.2 respectively, with $\mathcal{L} = 3$ in both cases. We give in Tab. 4 the data obtained for the confocal

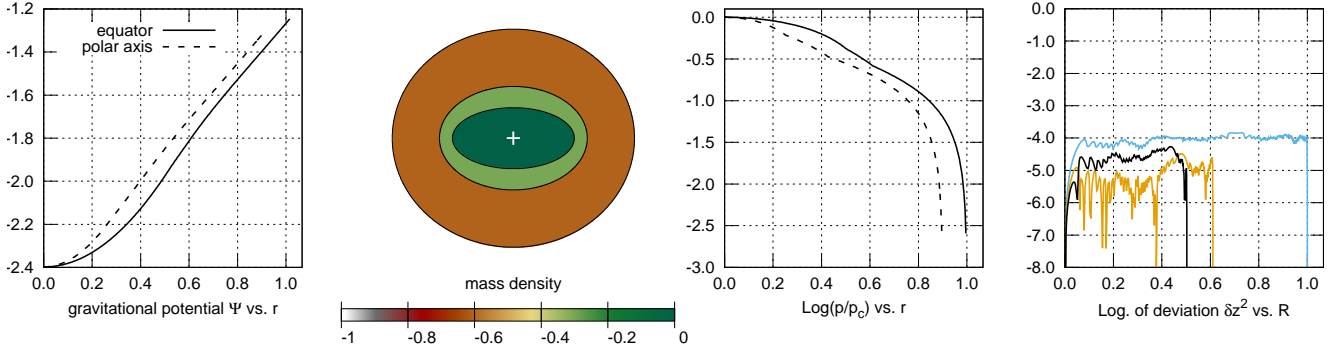


Figure 4. Same legend as for Fig. 2 but for configuration B (confocal case). See Tab. 4 for input/output parameters.

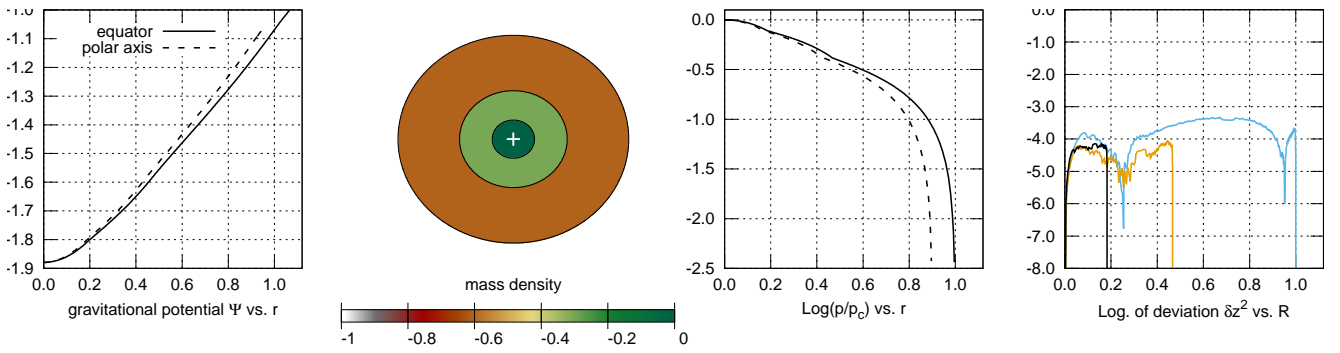


Figure 5. Same legend as for Fig. 2 but for configuration C (coelliptical case). See Tab. 5 for input/output parameters.

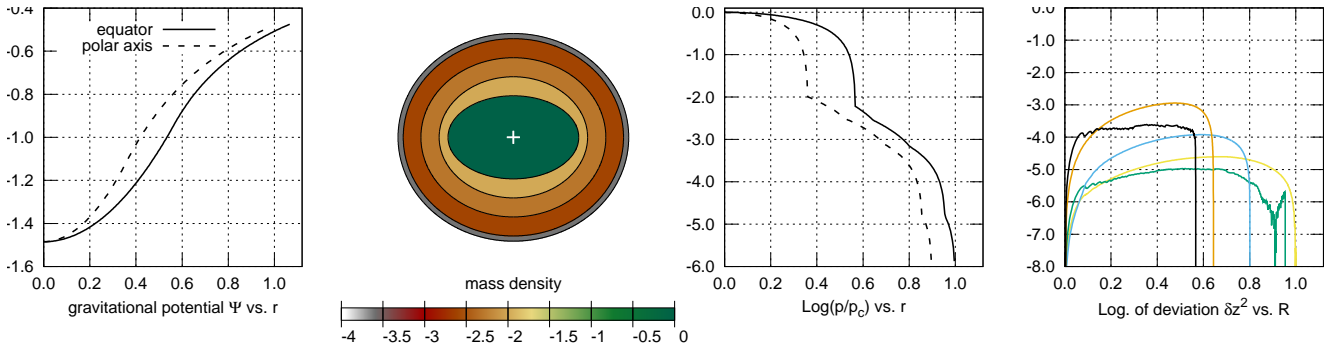


Figure 6. Same legend as for Fig. 2 but for configuration D (dense, rapidly-rotating interior). See Tab. 6 for input/output parameters.

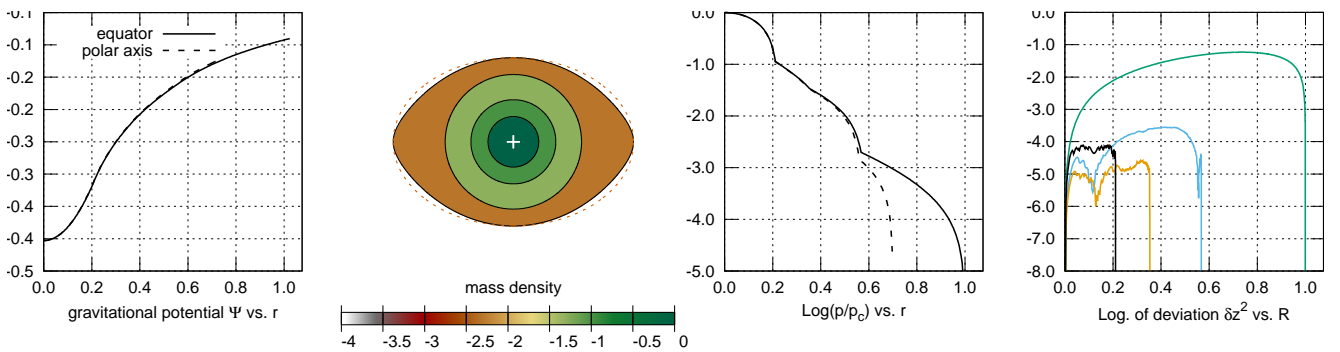


Figure 7. Same legend as for Fig. 2 but for configuration E (dense, slowly-rotating interior). See Tab. 7 for input/output parameters. The outer ellipse is shown (red, dot line).

configuration C (input)			
layer	$i = 1$	2	3
$q_{i,3\bar{\epsilon}_i}$	0.165	0.42	0.9
α_i	2	2	

configuration D (input)					
layer	$i = 1$	2	3	4	5
$q_{i,5\bar{\epsilon}_i}$	0.36	0.525	0.69	0.855	0.9
α_i	10^2	2	2	10	

	DROP-code	this work	
$q_{1,3}$	0.18309	0.18333	
$q_{2,3}$	0.46650	0.46666	
ϵ_1	0.43346	0.43588	
ϵ_2	0.43526	0.43588	
$c_{1,3}$	-0.18370	-0.18361	
$c_{2,3}$	-0.14877	-0.14862	
$V/a_{\mathcal{L}}^3$	3.76893	3.76991	
$p_c/\pi G\rho_3 a_3^2$	1.46945	1.46956	
$p_1^*/\pi G\rho_3 a_3^2$	1.15414	1.15434	
$p_2^*/\pi G\rho_3 a_3^2$	0.62076	0.62086	
$\tilde{\Omega}_1^2$	0.15008	0.15004	0.14559 ^a
$\tilde{\Omega}_2^2$	0.09200	0.09197	0.08932 ^a
$\tilde{\Omega}_3^2$	0.06533	0.06531	0.06338 ^a
$M/\rho_3 a_3^3$	4.19840	4.19950	
ν_1	0.02213	0.0223	
ν_2	0.17141	0.17139	

*value on the polar axis

^afrom (53) and (54)

Table 5. Same legend as for Tab. 1 but for configuration C (coelliptical case, $\mathcal{L} = 3$) shown in Fig. 5.

case. Here, the mass-density jumps and the ellipticities are the same for both methods. The fractional radii injected in the formula are easily computed from (13). This is configuration B. The pressure, the mass density and the deviations between bounding surfaces are displayed in Fig. 4. The parameter set and the results for the coelliptical configuration are listed in Tab. 5 and the associated plots are in Fig. 5. The procedure is similar: the location of points A_i and the mass-density jumps are imposed for both methods, which determines the unique ellipticity (this value is imposed by the outermost spheroid, namely $\bar{\epsilon} = OA_{\mathcal{L}}/OB_{\mathcal{L}}$). This is configuration C. Again, we see that the two techniques give very similar results with a precision better than 10^{-3} in relative on the main quantities. By changing slightly the input parameters, the code can deliver yet smaller confocal parameters.

In the fourth example, we consider a very dense (by a factor 10^2), rapidly (by a factor 10) rotating core surrounded with 4 low-mass layers in relative motion. The parameters are given in Tab. 6. This is configuration D. The pressure, the mass density and the deviations between surfaces are given in Fig. 6. The deepest layer is significantly flattened by rotation, as we have chosen $\bar{\epsilon}_1 \approx 0.64$ (this value is below the threshold of dynamical stability for single body). The formulas are fed with the fractional radii and ellipticities output by the simulation. The mass-density jumps are the same. As the table shows (column 2 and 3), the numerical SCF-method and the actual formalism compare very well, at a precision level of a few 10^{-3} typically. The confocal parameters are all very small, and much smaller than in previous examples. Note that we are far from a situation with small ellipticities.

The last example is some kind of reverse situation. The

	DROP-code	this work	
ϵ_1	0.77201	0.77211	
ϵ_2	0.57804	0.57804	
ϵ_3	0.50905	0.50906	
ϵ_4	0.44510	0.44510	
$q_{1,5}$	0.56639	0.56650	
$q_{2,5}$	0.64338	0.64337	
$q_{3,5}$	0.80163	0.80164	
$q_{4,5}$	0.95479	0.95479	
$c_{1,5}$	+0.00120	+0.00132	
$c_{2,5}$	-0.05168	-0.05169	
$c_{3,5}$	-0.023487	-0.02346	
$c_{4,5}$	-0.00938	-0.00938	
V/a_5^3	3.77000	3.76991	
$p_c/\pi G\rho_5 a_5^2 \times 10^{-6}$	1.92418	1.92191	
$p_1^*/\pi G\rho_5 a_5^2 \times 10^{-4}$	1.95711	1.95671	
$p_2^*/\pi G\rho_5 a_5^2 \times 10^{-4}$	0.58740	0.58659	
$p_3^*/\pi G\rho_5 a_5^2 \times 10^{-4}$	0.15143	0.15121	
$p_4^*/\pi G\rho_5 a_5^2 \times 10^{-4}$	0.00323	0.00322	
$\tilde{\Omega}_1^2 \times 10^{-2}$	6.77290	6.77090	6.35370 ^a
$\tilde{\Omega}_2^2 \times 10^{-2}$	0.67729	0.67482	0.82996 ^a
$\tilde{\Omega}_3^2 \times 10^{-2}$	0.45152	0.45059	0.59140 ^a
$\tilde{\Omega}_4^2 \times 10^{-2}$	0.30101	0.30045	0.40741 ^a
$\tilde{\Omega}_5^2 \times 10^{-2}$	0.27365	0.27317	0.37262 ^a
$M/\rho_5 a_5^3 \times 10^{-3}$	1.98941	1.98634	
ν_1	0.97462	0.97453	
$\nu_2 \times 10^2$	0.84950	0.85855	
$\nu_3 \times 10^2$	0.95480	0.95361	
$\nu_4 \times 10^2$	0.70774	0.70862	

*value on the polar axis

^afrom (53) and (54)

Table 6. Same legend as for Tab. 1 but for configuration D (type-V solution, massive and rapidly rotating core) shown in Fig. 6.

axis ratio of the outermost layer is set to 0.7, and its rotation rate is much larger than that of the dense core (by a factor 100). As above, the characteristics of the surface computed from the code are used as parameters for the analytical approach. The input parameters and output data are gathered in Tab. 7. This is configuration E, which is displayed in Fig. 7. The outer layer is especially flattened by centrifugation while the core is very close to spherical. This example also shows the limit in the model. This is indicated by the confocal parameters $c_{i\mathcal{L}}$ which are quite “large”. Besides, we see that the outer layer deviate significantly from a spheroid, namely by more than 10% beyond $R/a_{\mathcal{L}} \gtrsim 0.2$. The actual formalism, to be valid, not only requires $c_{i,j} \rightarrow 0$ but also that each bounding surface must be close to a spheroid, which property is not represented only by the $q_{i,j}$ ’s and ϵ_i ’s.

5 NOTE ON TYPE-C SOLUTIONS (GLOBAL ROTATION)

For $\mathcal{L} = 2$ (see Paper I), when the pressure is constant all along the interface E_1 between the embedded spheroid and

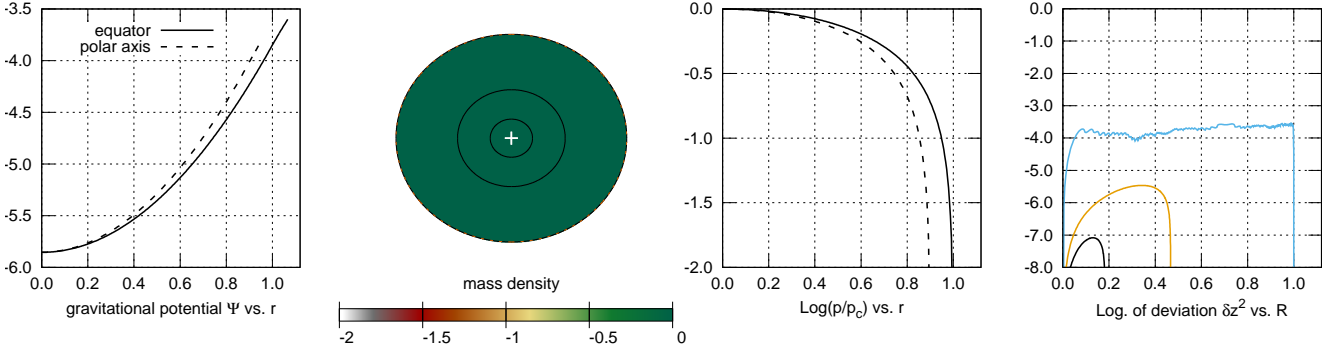


Figure 8. Same legend as for Fig. 2 but for configuration G (type-C solution; coelliptical case). See Tab. 9 for input/output parameters.

configuration E (input)				
layer	$i = 1$	2	3	4
$q_{i,4}\epsilon_i$	0.21	0.35	0.56	0.7
α_i	10	2	10	

	DROP-code	this work	
$q_{1,4}$	0.21082	0.21082	
$q_{2,4}$	0.35325	0.35327	
$q_{3,4}$	0.56738	0.56748	
ϵ_1	0.08837	0.08859	
ϵ_2	0.13546	0.13594	
ϵ_3	0.16083	0.16184	
$c_{1,4}$	-0.50965	-0.50965	
$c_{2,4}$	-0.50771	-0.50769	
$c_{3,4}$	-0.50167	-0.50156	
V/a_4^3	2.61819	2.93215	
$p_c/\pi G\rho_4 a_4^2 \times 10^{-3}$	1.33540	1.33388	
$p_1^*/\pi G\rho_4 a_4^2 \times 10^{-3}$	0.15182	0.15180	
$p_2^*/\pi G\rho_4 a_4^2 \times 10^{-3}$	0.04533	0.04532	
$p_3^*/\pi G\rho_4 a_4^2 \times 10^{-3}$	0.00191	0.00192	
$\tilde{\Omega}_1^2 \times 10^{-2}$	0.02265	0.03742	0.12355 ^a
$\tilde{\Omega}_2^2 \times 10^{-2}$	0.22659	0.21565	0.25293 ^a
$\tilde{\Omega}_3^2 \times 10^{-2}$	0.22659	0.21308	0.20310 ^a
$\tilde{\Omega}_4^2 \times 10^{-2}$	2.26594	2.26783	1.41244 ^a
$M/\rho_4 a_4^3$	18.28944	18.59843	
ν_1	0.42828	0.42045	
ν_2	0.15719	0.15471	
ν_3	0.31262	0.30778	

*value on the polar axis

^afrom (53) and (54)

Table 7. Same legend as for Tab. 1 but for configuration E (type-V solution, slowly-rotating core) shown in Fig. 7.

the host, then the two layers share the same rotation rate (solutions are then called “type-C” solutions). But the mass-density jump at E_1 is not arbitrary. In contrast, when the pressure varies with the cylindrical radius R — the variation is quadratic for rigid rotations —, then Ω differs from one layer to other. We have in this case “type-V” solutions. This is possible only if a mass-density jump $\alpha_1 \neq 1$ is present at the interface; see also [Basillais & Huré \(2021\)](#). These two classes of solutions also exist for $\mathcal{L} > 2$. Actually, the series of rotation rates obtained from (42) do not assign a unique value to all $\tilde{\Omega}'_i$ s, unless a “fortunate” selection of the input

parameters. Each layer has therefore its own rotation rate Ω_i . In this sense, (42) delivers type-V solutions in general. When rotation is global, i.e. $\tilde{\Omega}_i = \tilde{\Omega}$ for all i , then we have from (32) and (33), assuming $\alpha_i - 1 \neq 0$

$$\tilde{\Omega}^2 = -\mathcal{M}(\epsilon_j) \mathbf{X} \cdot [\mathbf{P}(B_j) + \mathbf{C}(A_j, B_j)], \quad j \in [1, \mathcal{L}]. \quad (47)$$

It follows that the mass density jumps α_i , the ellipticities ϵ_i and the fractional sizes $q_{i,j}$ are linked together. We see that $\tilde{\Omega}^2$ can be eliminated, for instance by subtracting each equation by the last one. We then get a *linear system of $\mathcal{L} - 1$ equations*, where the first $\mathcal{L} - 1$ components X_i of vector \mathbf{X} are the unknown (ϵ_i and $q_{i,j}$ are fixed in the procedure). This system of equations takes the form

$$\sum_{i=1}^{\mathcal{L}-1} D_{i,j} X_j - D_{\mathcal{L},j} = 0, \quad j \in [\mathcal{L} - 1], \quad (48)$$

where the matrix elements are given by

$$D_{i,j} = \mathcal{M}(\epsilon_j) [P_i(B_j) + C_i(A_j, B_j)] - \mathcal{M}(\epsilon_{\mathcal{L}}) [P_i(B_{\mathcal{L}}) + C_i(A_{\mathcal{L}}, B_{\mathcal{L}})], \quad (49)$$

and the second member is obtained for $i = \mathcal{L}$, namely

$$D_{\mathcal{L},j} = \mathcal{M}(\epsilon_j) [P_{\mathcal{L}}(B_j) + C_{\mathcal{L}}(A_j, B_j)] - \mathcal{M}(\epsilon_{\mathcal{L}}) [P_{\mathcal{L}}(B_{\mathcal{L}}) + C_{\mathcal{L}}(A_{\mathcal{L}}, B_{\mathcal{L}})]. \quad (50)$$

This system is easily solved numerically by standard techniques. The mass-density jumps associated with the solution \mathbf{X} are denoted α_{C_i} in the following.

As examples of type-C solutions, we have reconsidered configurations A, B and C discussed in Sect. 4.3 by conserving the same geometrical parameters, namely the fractional radii $q_{i\mathcal{L}}$ and ellipticities ϵ_i , while the mass-density jumps are deduced from (48). For parameters of configuration A (see Tab. 1), we find $X_1 \approx 3.71658$, $X_2 \approx 2.03476$ and $X_3 \approx 0.97393$, which yields $\alpha_{C1} \approx 1.92825$, $\alpha_{C2} \approx 2.02834$ and $\alpha_{C3} \approx 1.97393$. We call this new configuration F. The output quantities are reported in Tab. 8. Regarding parameters of configuration B (confocal state), (48) admits $X_1 \approx 2.65560$ and $X_2 \approx -2.77502$ as the solution, which leads to $\alpha_{C1} \approx 0.88057$ and $\alpha_{C2} \approx -1.77502$. This is therefore not a relevant physical state. For parameters of configuration C (coelliptical case), we find $\mathbf{X} = \mathbf{0}$, which means that all layers have the same mass density, and are therefore indistinguishable (this is a single body). We call this new configuration G. The results are listed in Tab. 9. The structure and the deviations between surfaces are displayed in Fig. 8

configuration F (input)					configuration G				
layer	$i = 1$	2	3	4	layer	$i = 1$	2	3	
$q_{i,4}\bar{\epsilon}_i$	0.21	0.45	0.72	0.9	$q_{i,3}\bar{\epsilon}_i$	0.165	0.42	0.9	
		DROP-code	this work				DROP-code	this work	
$q_{1,4}$			0.22176		$q_{1,3}$		0.18334	0.18333	
$q_{2,4}$			0.48230		$q_{2,3}$		0.46669	0.46666	
$q_{3,4}$			0.78690		ϵ_1		0.43599	0.43588	
ϵ_1			0.32141		ϵ_2		0.43600	0.43588	
ϵ_2			0.35984		$c_{1,3}$		-0.18361	-0.18361	
ϵ_3			0.40349		$c_{2,3}$		-0.14859	-0.14862	
$c_{1,4}$			-0.18491		$V/a_{\mathcal{L}}^3$		3.77310	3.76991	
$c_{2,4}$			-0.15987		$p_c/\pi G\rho_3 a_3^2$		0.58626	0.58615	
$c_{3,4}$			-0.08918		$p_1^*/\pi G\rho_3 a_3^2$		0.56656	0.56645	
α_1		2	1.92825		$p_2^*/\pi G\rho_3 a_3^2$		0.45861	0.45850	
α_2		2	2.02834		$\tilde{\Omega}$		0.05208	0.05202	
α_3		2	1.97393		$M/\rho_{\mathcal{L}} a_{\mathcal{L}}^3$		3.77311	3.76991	
$V/a_{\mathcal{L}}^3$		3.76482	3.76991		ν_1		0.00641	0.00616	
$p_c/\pi G\rho_4 a_4^2$		6.22120	6.01587		ν_2		0.09560	0.09546	
$p_1^*/\pi G\rho_4 a_4^2$		4.23392	4.16533						
$p_2^*/\pi G\rho_4 a_4^2$		1.89159	1.85745						
$p_3^*/\pi G\rho_4 a_4^2$		0.45253	0.44881						
$\tilde{\Omega}_1^2$		0.13002	0.12900						
$\tilde{\Omega}_2^2$		0.13002	0.12900						
$\tilde{\Omega}_3^2$		0.13002	0.12900						
$\tilde{\Omega}_4^2$		0.13002	0.12900						
$M/\rho_4 a_4^3$		6.68126	6.68742						
ν_1		0.05178	0.05175						
ν_2		0.23664	0.23639						
ν_3		0.42743	0.42737						

*value on the polar axis

Table 8. Same legend as for Tab. 1 but for configuration F (type-C solution) associated with the same geometrical parameters as for configuration A; see Tab. 1. The mass-density jumps are found by solving (48), which ensures that all layers rotates at the same rate.

6 APPROXIMATIONS FOR SMALL ELLIPTICITIES

Ellipticities close to zero are generally associated with states of low rotation. As in Paper I, we can expand each component of $\mathbf{P}(\mathbf{B}_j)$ in $\epsilon_i \ll 1$. It is easy to show that

$$\mathcal{M}(x)\mathcal{P}(x,y) \approx -\frac{2}{3}\left(x^2 - \frac{3}{5}y^2\right), \quad (51)$$

for $x \ll 1$ and $y \ll 1$. So, if we define $\sqrt{k_{ij}} = \epsilon_i/\epsilon_j$, the components of $\mathcal{M}(\epsilon_j)\mathbf{P}(\mathbf{B}_j)$ can be approximated by

$$\mathcal{M}(\epsilon_j)\mathbf{P}_i(\mathbf{B}_j) \approx \frac{2}{15} \times \begin{cases} \epsilon_i^2(3q_{i,j}^2 - 5k_{j,i})q_{i,j}^3, & \text{for } i < j, \\ \epsilon_j^2(-5 + 3k_{i,j}), & \text{for } i \geq j. \end{cases} \quad (52)$$

This separation comes directly from (30). Actually, we have $\mathbf{P}_i(\mathbf{B}_j) = f_{i,j}\mathcal{P}(\epsilon_j, \epsilon'_{i,j})$ for $i < j$, while this component becomes $\mathcal{P}(\epsilon_j, \epsilon_i)$ for $i \geq j$. Under these conditions, and omitting the first-order correction represented by vector \mathbf{C} , (32)

Table 9. Same legend as for Tab. 1 but for configuration G (type-C solution) shown in Fig. 8, associated with the same geometrical parameters as for configuration C; see Tab. 5.

becomes

$$\tilde{\Omega}_{\mathcal{L}}^2 \approx \frac{4}{15}\epsilon_{\mathcal{L}}^2 - \frac{2}{15} \sum_{i=1}^{\mathcal{L}-1} \epsilon_i^2 \tilde{\rho}_{i+1}(\alpha_i - 1)(3q_{i,\mathcal{L}}^2 - 5k_{\mathcal{L},i})q_{i,\mathcal{L}}^3. \quad (53)$$

For internal layers $j \in [1, \mathcal{L} - 1]$, we use (33). If we separate the summation into two parts (see Sect. 2.2), we have

$$\alpha_j \tilde{\Omega}_j^2 \approx \tilde{\Omega}_{j+1}^2 - (\alpha_j - 1) \frac{2}{15} \left[\sum_{i=1}^{j-1} \epsilon_i^2 \tilde{\rho}_{i+1}(\alpha_i - 1)(3q_{i,j}^2 - 5k_{j,i})q_{i,j}^3 + \sum_{i=j}^{\mathcal{L}-1} \epsilon_j^2 \tilde{\rho}_{i+1}(\alpha_i - 1)(3k_{i,j} - 5) + \epsilon_j^2(3k_{\mathcal{L},j} - 5) \right], \quad (54)$$

where the last term inside the brackets corresponds to $i = \mathcal{L}$, i.e. the last components in (29) and (30). Note that, for $j = 1$, the first summation is absent. We give in Tabs. 1 to 7 the series of rotation rates computed from (53) and (54) for configurations A to E considered above. We see that these zero-order formula are sufficient to get a precision of the order of a few percents. Unsurprisingly, it fails when the confocal parameters are not small in absolute compared to unity (this assumption underlies the present formalism as a whole), which is clearly the case of configuration E. Configurations, like examples D and E, with large mass-density jumps are also poorly reproduced. This is inherent in the formula where the α_i 's magnify the errors.

7 SUMMARY AND PERSPECTIVES

In this article, we have investigated the conditions under which a self-gravitating structure made of \mathcal{L} nested layers

in relative rotation be in equilibrium (under axial and equatorial symmetries). It generalizes the approach considered in Paper I focused on the two-layer case. There are three main assumptions, namely: i) all layers are separated by concentric, spheroidal (non-intersecting) surfaces, ii) each layer is homogeneous, and iii) each layer can rotate at its own rate. Assumptions i) and ii) enable to use exact results from potential theory (Chandrasekhar 1969; Binney & Tremaine 1987). We have shown that the problem admits approximate solutions compatible with rigid rotation provided confocal parameters $c_{i,j}$ are close to zero (in the limit $c_{i,j} \rightarrow 0$, these solutions are exact, according to Poincaré’s theorem; see the Introduction). Then, the full sequence of rotation rates $\Omega_1, \dots, \Omega_{\mathcal{L}}$ can be generated from recursion; see (32) and (33). A similar procedure leads to the interface pressures along the polar axis and to the central pressure; see the Appendix A. There are $3\mathcal{L}-2$ input parameters in total, namely the ellipticities $\epsilon_i \in [0, 1]$, the fractional radii $q_{i,\mathcal{L}} \in [0, 1]$ and the mass-density jumps $\alpha_i \in [1, \infty[$ at the interfaces (other options are possible). The approach is vectorial, totally scale free, and is easily implemented in practice; see, for instance, the Appendix C for a basic Fortran 90 code. As discussed, any set of input parameters does not necessarily lead to a physical solution. Actually, all the Ω_i^2 ’s must be positive values, which is difficult to guarantee without considering numbers in the formulas (the number of input parameters determines the size of the parameter space). Nevertheless, we have qualitatively shown that the most favorable conditions for getting solutions are met for a positive ellipticity gradient outward (the layer are more and more oblate from centre to surface, at the opposite of confocal configurations). In general, the physical solution corresponds to layers in relative motion (i.e. type-V solutions), unless some specific choices of the input parameters. States where all rotation rates coincide (rotation is global; type-C solutions) are directly accessible by solving a linear system of $\mathcal{L} - 1$ equations, where the mass-density jumps become the unknowns (the ϵ_i ’s and the $q_{i,\mathcal{L}}$ ’s are still parameters). Global rotation is therefore more constrained (and less numerous) than asynchronous states. In particular, we have demonstrated that confocal configurations are not possible in the presence of a negative mass-density gradient outward (no density inversion). This reinforces the conclusion by Hamy (1890) and Montalvo et al. (1983). In a similar manner, we have shown that coelliptical configurations are not possible for global rotation, which prolongates Hamy’s theorem limited to small ellipticities. Of particular interest is the case of small ellipticities, which applies to slowly-rotating stars and planets. In this purpose, the recursion formula, expanded in $\epsilon_i^2 \ll 1$, takes a simple form. The formalism has been widely tested through examples by using the numerical SCF-method as the reference. It turns out that, provided the confocal parameters are small enough, namely $c_{i,j}^2 \ll 1$, then the precision of the method easily reaches 10^{-3} in relative, which should be sufficient for most applications.

The formalism can help in better understanding the internal structure (number of representative layers, ellipticities, fractional radii and mass-densities) of stars and planets from observational data (mass, shape, rotation rate, gravitational moments, etc.). Note that many models of planetary interiors are based on coelliptical configurations and global rotation (e.g. Schubert et al. 2011;

Hubbard 2013; Nettelmann 2017; Debras & Chabrier 2018), which are clearly forbidden; see also Cisneros-Parra et al. (2017). By releasing the constraints in the ellipticities of layers (e.g. Zhang 1996) — more drastically, in their shape (Nettelmann et al. 2021) —, and by allowing different rotation rates (e.g. Cisneros-Parra et al. 2020), the observational data might be easily reproduced by a very limited number of homogeneous layers. An application to Jupiter is currently underway.

The paper opens onto a few exciting (eventually old) problems. This is, for instance, the determination of equilibrium sequences for various equations of states (like polytropic ones, for instance). Actually, in the limit $\mathcal{L} \rightarrow \infty$, the relationship between the α_i ’s, the series of ellipticities, fractional mass, and the polytropic index should be accessible. Then, a connection with the solution of the Lane-Emden equation in the limit $\epsilon_i \rightarrow 0$ and solution might be also established. Another question concerns the assumption of non-intersecting surfaces, as considered for instance by Abramyan & Kaplan (1974) and Caimmi (1986). Which conditions are required to get polar caps or equatorial caps? This may be interesting in the context of exoplanets and ocean planets. It could also be very interesting to consider the existence of nested figures involving prolate spheroidal surface, which may occur, for instance, in the presence of circulation of magnetic field (Kawamura et al. 2011; Fujisawa & Eriguchi 2014). As shown here, rapidly rotating layers tend to produce quasi-spherical cores (see, for instance, configuration E).

DATA AVAILABILITY

All data are incorporated into the article.

ACKNOWLEDGEMENTS

I am grateful to the referee for his very precise report, and in particular for checking all the formulas, which has permitted to remove several typos. I would like to thank E. Di Folco for many interesting discussions about applications, B. Basillais and C. Staelen for testing the recurrence formulas in practical cases.

REFERENCES

- Abramyan M. G., Kaplan S. A., 1974, *Astrophysics*, 10, 358
- Basillais B., Huré J. M., 2021, *MNRAS*, 506, 3773
- Binney J., Tremaine S., 1987, *Galactic dynamics*. Princeton, NJ, Princeton University Press, 1987, 747 p.
- Caimmi R., 1986, *A&A*, 159, 147
- Caimmi R., 2016, *Applied Mathematical Sciences*, 10, 1821
- Chandrasekhar S., 1969, *Ellipsoidal figures of equilibrium*. Yale Univ. Press
- Cisneros-Parra J. U., Martínez-Herrera F. J., Montalvo-Castro J. D., 2020, *American Journal of Astronomy and Astrophysics*, 8, 8
- Cisneros-Parra J. U., Martínez-Herrera F. J., Montalvo-Castro J. D., 2017, *ApJ*, 848, 109
- Cisneros-Parra J. U., Martínez-Herrera F. J., Montalvo-Castro J. D., 2019, *ApJS*, 241, 8
- Clement M. J., 1974, *ApJ*, 194, 709

- Debras F., Chabrier G., 2018, *A&A*, 609, A97
 Fujisawa K., Eriguchi Y., 2014, *MNRAS*, 438, L61
 Hachisu I., 1986, *ApJS*, 62, 461
 Hamy M., 1889, *Annales de l'Observatoire de Paris*, 19, F.1
 Hamy M., 1890, *Journal de mathématiques pures et appliquées*.
 Tome VI. Gauthier-Villars et Fils
 Horedt G. P., ed. 2004, *Polytropes - Applications in Astrophysics and Related Fields* Vol. 306 of *Astrophysics and Space Science Library*
 Hubbard W. B., 2013, *ApJ*, 768, 43
 Huré J. M., 2021, submitted to *MNRAS* (Paper I)
 Jeans J. H., 1928, *Astronomy and cosmogony*
 Kadam K., Motl P. M., Frank J., Clayton G. C., Marcello D. C., 2016, *MNRAS*, 462, 2237
 Kawamura T., Taniguchi K., Yoshida S., Eriguchi Y., 2011, *MNRAS*, 416, L75
 Kiuchi K., Nagakura H., Yamada S., 2010, *ApJ*, 717, 666
 Love A., Appell P., Beghin H., Villat H., 1914, *Encyclopédie des sciences mathématiques pures et appliquées*. Tome IV. Cinquième volume. Fascicule 2. 18.4. Les grands classiques Gauthier-Villars, J. Gabay, Sceaux
 Lyttleton R., 1953, *The Stability of Rotating Liquid Masses*. University Press
 Maeder A., 1971, *A&A*, 14, 351
 Maeder A., 2009, *Physics, Formation and Evolution of Rotating Stars*
 Montalvo D., Martinez F. J., Cisneros J., 1983, *Rev. Mex. Astron. Astrofis.*, 5, 293
 Nettelmann N., 2017, in *AGU Fall Meeting Abstracts* Vol. 2017, Low- and high-order gravitational harmonics of interior models for rigidly rotating Jupiter. pp P31C-2809
 Nettelmann N., Movshovitz N., Ni D., Fortney J. J., Galanti E., Kaspi Y., Helled R., Mankovich C. R., Bolton S., 2021, *arXiv e-prints*, p. arXiv:2110.15452
 Poincaré H., 1888, *Comptes rendus des séances de l'académie des sciences*. Tome 106. Gauthier-Villars et Fils
 Rambaux N., Chambat F., Castillo-Rogez J. C., 2015, *A&A*, 584, A127
 Schönberg M., Chandrasekhar S., 1942, *ApJ*, 96, 161
 Schubert G., Anderson J., Zhang K., Kong D., Helled R., 2011, *Physics of the Earth and Planetary Interiors*, 187, 364
 Tohline J. E., 2021, a (MediaWiki-based) *Vistrails.org* publication, <https://www.vistrails.org/index.php/User:Tohline>
 Véronet A., 1912, *Journal de mathématiques pures et appliquées* 6e série, 8, 331
 Zhang C. Z., 1996, *Earth Moon and Planets*, 75, 17

APPENDIX A: INTERFACE PRESSURES ON THE POLAR AXIS

As for the rotation rates, we proceed from the top layer down to the deepest one. The pressure on the polar axis is easily found since there is no centrifugal force at $R = 0$. The pressure at the poles are denoted $p_i(A_i) \equiv p_i^*$. By using (4) for a given layer $j + 1$ at E_j (bottom surface) and E_{j+1} (top surface), we get

$$\frac{1}{\rho_{j+1}} (p_{j+1}^* - p_j^*) + \Psi(E_{j+1}, 0) - \Psi(E_j, 0) = 0, \quad (\text{A1})$$

for $i = 1, \mathcal{L} - 1$. We have $p_{\mathcal{L}} = 0$ along $E_{\mathcal{L}}$ and in particular at point $A_{\mathcal{L}}$, which initializes the recursivity. By using (14), the above formula therefore reads

$$\begin{cases} p_{\mathcal{L}}^* = 0, \\ p_j^* = p_{j+1}^* + \rho_{j+1} [\Psi(E_{j+1}, 0) - \Psi(E_j, 0)], \end{cases} \quad (\text{A2})$$

with $j \in [1, \mathcal{L} - 1]$, and

$$\frac{\Psi(E_j, 0)}{-\pi G a_j^2} = \sum_{i=1}^{\mathcal{L}-1} (\rho_i - \rho_{i+1}) \{ f_{i,j} [A_0(\epsilon'_{i,j}) x_{i,j} - A_3(\epsilon'_{i,j}) \bar{\epsilon}_j^2] \Big|_{A_j} + \rho_{\mathcal{L}} [A_0(\epsilon'_{\mathcal{L},j}) x_{\mathcal{L},j} - A_3(\epsilon'_{\mathcal{L},j}) \bar{\epsilon}_j^2] \}. \quad (\text{A3})$$

The central pressure p_c is obtained in a similar way, from

$$p_c = p_1^* + \rho_1 [\Psi(E_1, 0) - \Psi_c], \quad (\text{A4})$$

where Ψ_c is the potential at the origin of coordinates which is found from (9), namely

$$\frac{\Psi_c}{-\pi G a_{\mathcal{L}}^2} = \sum_{i=1}^{\mathcal{L}-1} (\rho_i - \rho_{i+1}) f_{i,j} A_0(\epsilon'_{i,j}) x_{i,j} + \rho_{\mathcal{L}} A_0(\epsilon'_{\mathcal{L},j}) x_{\mathcal{L},j}. \quad (\text{A5})$$

Note that the mass density jumps can easily be introduced by dividing this expression by $\rho_{\mathcal{L}}$

APPENDIX B: THE TWO-LAYER CASE

For $\mathcal{L} = 2$, (29), (30) and (31) reduce to

$$\mathbf{X} = \begin{pmatrix} \alpha_1 - 1 \\ 1 \end{pmatrix}, \quad (\text{B1})$$

$$\mathbf{P}(B_j) = \begin{pmatrix} f_{1,j} \mathcal{P}(\epsilon_j, \epsilon'_{1,j}) \Big|_{B_j} \\ \mathcal{P}(\epsilon_j, \epsilon_2) \end{pmatrix}, \quad (\text{B2})$$

and

$$\mathbf{C}(A_j, B_j) = \begin{pmatrix} f_{1,j} \mathcal{C}(\epsilon_j, \epsilon'_{1,j}) \Big|_{A_j}^{B_j} \\ 0 \end{pmatrix}, \quad (\text{B3})$$

where $j \in \{1, 2\}$. Then, for $j = 2$ (i.e. the outer layer), we have $\mathcal{P}(\epsilon_2, \epsilon_2) = -1$, and (32) leads to

$$\tilde{\Omega}_2^2 = \mathcal{M}(\epsilon_2) \left\{ 1 - (\alpha_1 - 1) \left[f_{1,2} \mathcal{P}(\epsilon_2, \epsilon'_{1,2}) \Big|_{B_2} + f_{1,2} \mathcal{C}(\epsilon_2, \epsilon'_{1,2}) \Big|_{A_2}^{B_2} \right] \right\}, \quad (\text{B4})$$

where $\epsilon'_{1,2}$ is to be replaced by $q_{1,2} \epsilon_1$ at point B_2 , and by $\frac{q_{1,2} \epsilon_1}{\sqrt{1-c_{1,2}}}$ at point A_2 . For the embedded ellipsoid, we set $j = 1$ in (33), which leads to

$$\alpha_1 \tilde{\Omega}_1^2 = \tilde{\Omega}_2^2 + (\alpha_1 - 1) \mathcal{M}(\epsilon_1) [\alpha_1 - 1 - \mathcal{P}(\epsilon_1, \epsilon_2)]. \quad (\text{B5})$$

Note the absence of term \mathcal{C} in this last relationship since E_1 is interior to E_2 and it is confocal with itself. We therefore recover the expressions reported in Paper I. It can be shown that (53) and (54) are also on accordance.

APPENDIX C: F90 PROGRAM

Not optimized. Routines cteA0(e), cteA1(e), and cteA3(e) are required (see Paper I).

```

Program nsfoel
  ! gfortran nsfoel.f90; ./a.out
  Implicit None
  Integer,Parameter::AP=Kind(1.00E+00),N_LAYER=4
  Real(Kind=AP),Parameter::PI=Atan(1._AP)*4
  Real(Kind=AP),dimension(1:N_LAYER)::alpha,e,ebar,q,om2
  ! Statements
  ! input parameters L, qi's, ei's, alphai's (setup for configuration A)
  q(1:N_LAYER)=(/2.2176752446908443E-01_AP,4.8230874759281428E-01_AP,7.8690212732359022E-01_AP,1._AP/)
  alpha(1:N_LAYER)=(/2._AP,2._AP,2._AP,1._AP/)
  ebar(1:N_LAYER)=(/0.21_AP,0.45_AP,0.72_AP,0.9_AP)/q(1:N_LAYER)
  e(1:N_LAYER)=Sqrt(1._AP-ebar(1:N_LAYER)**2)
  print*,"Ellipticities EPSILON(1:L)",e(1:N_LAYER)
  print*,"Fractional sizes q(1:L-1)",q(1:N_LAYER-1)
  print*,"Mass density jumps ALPHA(1:L-1)",alpha(1:N_LAYER-1)
  ! TYPE-V SOLUTION
  ! input: N_LAYER,e(1:N_LAYER),q(1:N_LAYER),alpha(1:N_LAYER)
  ! output: om2(1:N_LAYER)
  Call NFEL_typeV_Solution(N_LAYER,e(1:N_LAYER),q(1:N_LAYER),alpha(1:N_LAYER),om2(1:N_LAYER))

```

Contains

```

Subroutine NFEL_typeV_Solution(L,e,q,alpha,W2)
  Implicit none
  Integer,Intent(In)::L
  Real(Kind=AP),Dimension(1:L),Intent(In)::e,q,alpha
  Real(Kind=AP),Dimension(1:L),Intent(Out)::W2
  ! local
  Integer::I,J
  Real(Kind=AP),Dimension(1:L)::e2,ebar,rho,fvol,Avec,pif,psipole
  Real(Kind=AP),Dimension(1:L,1:L)::cij,xija,xijb,fija,fijb,eprimija,eprimijb,MPvec,MCvec
  Real(Kind=AP)::qij,mass,pc,psic
  ! initializations Ai's, rhoi's, qij's, xij's, fij's, e'ij's
  print*,"TYPE-V SOLUTION"
  e2(1:L)=e(1:L)**2;ebar(1:L)=Sqrt(1._AP-e2(1:L))
  rho(L)=1._AP;Avec(L)=1._AP
  Do I=L,1,-1
    If (I<L) then
      rho(I)=alpha(I)*rho(I+1);Avec(I)=rho(I)-rho(I+1)
    Endif
    Do J=1,L
      qij=q(I)/q(J)
      If (J>I) Then
        cij(I,J)=qij**2*e2(I)-e2(J)
        xijb(I,J)=1._AP;eprimijb(I,J)=qij*e(I)/Sqrt(xijb(I,J))
        fijb(I,J)=qij**3*ebar(I)/xijb(I,J)/sqrt(xijb(I,J)-qij**2*e2(I))
        xija(I,J)=1._AP+cij(I,J);eprimija(I,J)=qij*e(I)/Sqrt(xija(I,J))
        fija(I,J)=qij**3*ebar(I)/xija(I,J)/sqrt(xija(I,J)-qij**2*e2(I))
      Else
        cij(I,J)=0._AP
        xija(I,J)=qij**2;fija(I,J)=1._AP;eprimija(I,J)=e(I)
        xijb(I,J)=qij**2;fijb(I,J)=1._AP;eprimijb(I,J)=e(I)
      Endif
    Enddo
  Enddo
  print*,"Mass densities RHO(1:L)",rho(1:L)
  print*,"Confocal param. c(1:L-1,L)",cij(1:L-1,L)
  ! continued, Ai and M(ej).[Pi(Bj)+Ci(Aj,Bj)]
  psic=0._AP

```

```

Do J=1,L
  psipole(J)=-fija(L,J)*(cteA0(eprimija(L,J))*xija(L,J)-cteA3(eprimija(L,J))*(1._AP-e2(J)))
  Do I=1,L-1
    psipole(J)=psipole(J)&
      &-Avec(I)*fija(I,J)*(cteA0(eprimija(I,J))*xija(I,J)-cteA3(eprimija(I,J))*(1._AP-e2(J)))
    If (J>I) Then
      MPvec(I,J)=fijb(I,J)*(cteA3(eprimijb(I,J))*(1._AP-e2(J))-cteA1(eprimijb(I,J)))
      MCvec(I,J)=fijb(I,J)*(cteA0(eprimijb(I,J))*xijb(I,J)-(1._AP-e2(J))*cteA3(eprimijb(I,J)))&
        &-fija(I,J)*(cteA0(eprimija(I,J))*xija(I,J)-(1._AP-e2(J))*cteA3(eprimija(I,J)))
    Else
      MPvec(I,J)=cteA3(e(I))*(1._AP-e2(J))-cteA1(e(I));MCvec(I,J)=0._AP
    Endif
  Enddo
  psic=psic-Avec(J)*cteA0(e(J))*q(J)**2
  psipole(J)=psipole(J)*q(J)**2
Enddo
MPvec(L,1:L)=cteA3(e(L))*(1._AP-e2(1:L))-cteA1(e(L));MCvec(L,1:L)=0._AP
print*,"Interface potential PSI*(L:1) and central value PSIC",psipole(L:1:-1),psic
! sequence of rotation rates, TYPE-V SOLUTION
J=L
pif(J)=0._AP
W2(J)=-dot_product(Avec(1:L),MPvec(1:L,J)+MCvec(1:L,J))
Do J=L-1,1,-1
  fvol(J+1)=ebar(J+1)*q(J+1)**3-q(J)**3*ebar(J)
  W2(J)=(W2(J+1)-dot_product(Avec(1:L),MPvec(1:L,J)+MCvec(1:L,J)))*(alpha(J)-1._AP)/alpha(J)
  pif(J)=rho(J+1)*(psipole(J+1)-psipole(J))+pif(J+1)
Enddo
pc=rho(1)*(psipole(1)-psic)+pif(1)
print*,"Interface pressures p*(L:1) and central value pc",pif(L:1:-1),pc
fvol(1)=q(1)**3*ebar(1)
print*,"Rotation rates W2(1:L) (norm.)",W2(1:L)
mass=dot_product(fvol(1:L),rho(1:L))*PI*4/3
print*,"Total mass M",mass
print*,"Fractional masses NU(1:L)",fvol(1:L)*rho(1:L)/mass*PI*4/3
End Subroutine NFEL_typeV_Solution

End Program nsfoel

```